Chronic *in vivo* imaging in the mouse spinal cord using an implanted chamber

Matthew J Farrar[1,2], Ida M Bernstein[2], Donald H Schlafer[3], Thomas A Cleland[4], Joseph R Fetcho[5] & Chris B Schaffer[2]

Understanding and treatment of spinal cord pathology is limited in part by a lack of time-lapse *in vivo* imaging strategies at the cellular level. We developed a chronically implanted spinal chamber and surgical procedure suitable for time-lapse *in vivo* multiphoton microscopy of mouse spinal cord without the need for repeat surgical procedures. We routinely imaged mice repeatedly for more than 5 weeks postoperatively with up to ten separate imaging sessions and observed neither motor-function deficit nor neuropathology in the spinal cord as a result of chamber implantation. Using this chamber we quantified microglia and afferent axon dynamics after a laser-induced spinal cord lesion and observed massive microglia infiltration within 1 d along with a heterogeneous dieback of axon stumps. By enabling chronic imaging studies over timescales ranging from minutes to months, our method offers an ideal platform for understanding cellular dynamics in response to injury and therapeutic interventions.

In vivo optical imaging in the live mouse cortex has been achieved at depths of more than 1 mm with sub-micrometer resolution using nonlinear microscopy coupled with cranial window preparations[1]. This imaging approach has particular value for the study of neuropathology. For example, longitudinal studies (time-lapse imaging of the same region in the same animal over multiple days) in mouse models have relied on two-photon excited fluorescence (2PEF) microscopy to study the appearance and evolution of amyloid-β plaques in Alzheimer's disease[2–4], the rate and extent of amyloid-β clearance in response to antibody therapy[5], the diapedesis of circulating cancer cells and formation of metastatic tumors[6] as well as the long-term effects of occlusion and reperfusion of cerebral blood vessels[7]. In all cases, a surgical protocol enabling repeated optical access to the relevant tissue is a prerequisite to longitudinal studies. Existing protocols include an open-skull protocol[8] for a cranial window in which a small portion of the mouse skull is replaced with glass, thinned-skull preparations[9] and a recently described glass-reinforced, thinned-skull preparation[10].

Chronic optical imaging could offer comparable experimental advantages to the study of the spinal cord, including studies of spinal cord injury (SCI), spinal tumors, syringeomyelia, myelitis and spinal cord ischemia. For example, time-lapse *in vivo* studies of axon trajectories after SCI would enable unambiguous identification of spared, injured and regenerating axons and provide an ideal platform for evaluating therapies aimed at spurring axon growth. This approach has been demonstrated *in vivo* in zebrafish[11], where injured axons as well as axons that regenerated in response to therapy have been imaged over several days after SCI. Others have performed time-lapse fluorescence imaging in the spinal cord of mice expressing enhanced GFP (EGFP) in a subset of dorsal root ganglia (DRG) neurons for up to 72 h after SCI[12]. However, this imaging requires artificial ventilation and the suppression of breathing during image acquisition, limiting the timescale of cellular dynamics accessible. Similarly, 2PEF imaging in the spinal cord of mice expressing GFP in microglia has been demonstrated[13] with up to two imaging sessions in the same mouse separated by several days. Heavy sedation, whole-body suspension and local clamping are used to reduce remaining motion artifacts resulting from breathing and heartbeat. Similar techniques have been used to study microglia dynamics after a laser-induced microinjury[14], calcium signaling of dorsal horn neurons[15], the effects of peripheral nerve lesioning on sprouting of severed DRG axons[16] and experimental autoimmune encephalomyelitis[17]. Finally, imaging at as long as 4 months after SCI with as many as six imaging sessions in one subject has been achieved without interfering with animal breathing during imaging[18].

In all of these studies, obtaining images on days after the initial surgery is possible only by repeated surgical opening of the animal for each imaging session. Repeat surgeries increase the risk of infection, add a potentially confounding source of inflammation, cause tissue damage, cause additional pain and distress to the animal and severely limit the number of imaging time points possible. However, unlike the cranium, the relevant portions of the spine routinely flex and are close to the heart and lungs, requiring any chronic preparation to maintain the mechanical stability of the spine and minimize motion artifacts during imaging.

To provide a surgical preparation that enables repeated optical imaging of the mouse spinal cord without requiring repeated

[1]Department of Physics, Cornell University, Ithaca, New York, USA. [2]Department of Biomedical Engineering, Cornell University, Ithaca, New York, USA. [3]Department of Biomedical Sciences, Cornell University, Ithaca, New York, USA. [4]Department of Psychology, Cornell University, Ithaca, New York, USA. [5]Department of Neurobiology and Behavior, Cornell University, Ithaca, New York, USA. Correspondence should be addressed to C.B.S. (cs385@cornell.edu).

RECEIVED 10 MARCH 2011; ACCEPTED 8 DECEMBER 2011; PUBLISHED ONLINE 22 JANUARY 2012; DOI:10.1038/NMETH.1856

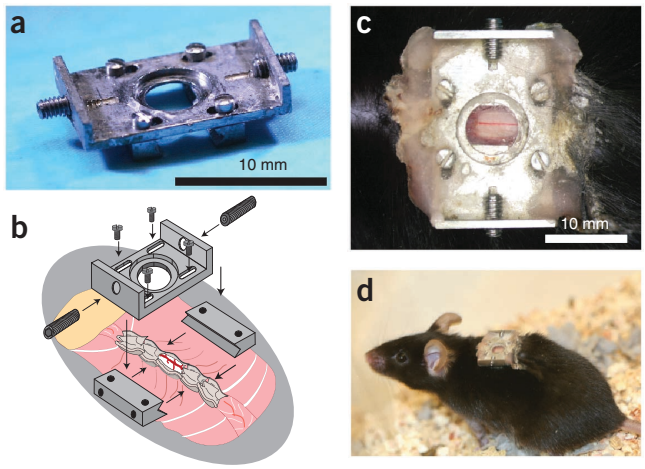

Figure 1 | An imaging chamber for longitudinal optical access to mouse spinal cord without the need for repeated surgeries. (**a**) Photograph of the imaging chamber. (**b**) Schema showing the implantation of the imaging chamber in mice at the T11–T12 vertebra, just below the dorsal fat pad (taupe). (**c**) Photograph showing the spinal cord imaged through the implanted chamber 144 d after the surgery. (**d**) Photograph of a mouse with an implanted chamber (same mouse as in **c**).

surgeries, we developed an implantable spinal chamber that provides continuous optical access to the mouse spinal cord. Using this chamber, we performed 2PEF imaging in transgenic mice expressing fluorescent proteins in microglia and afferent axons, and found axon morphology to be stable over 8 weeks of imaging. Standard tests of locomotor function did not show deficits in mice with the implant as compared to control mice. Postmortem histology did not show evidence of damage to the spinal cord from the surgery but revealed increases in microglia numbers in the dorsal portion of the spinal cord, consistent with mild inflammation. Finally, we imaged blood vessels, afferent axons and microglia after laser-induced microlesioning of the spinal cord using 2PEF microscopy and quantified microglial infiltration and axon 'dieback' dynamics on time scales spanning four orders of magnitude. We found that the increase in microglial density at the lesion site was fastest within the first 24 h after injury. Axon dieback rates were highly heterogeneous among axons, were fastest immediately after injury and slowed over 5 weeks after SCI.

RESULTS

The imaging chamber

The chamber consisted of two metal bars that attach to the spine together with a top plate that attaches to the bars and holds a glass window (**Fig. 1a**). The implantation procedure entailed retracting muscles and scraping clean the dorsal laminae over the imaging site, then fusing three vertebrae by clamping them on either side with small metal bars (**Fig. 1b**) held magnetically on fixed posts and finally performing a dorsal laminectomy with vanna scissors. We trimmed the lateral edges of the bone as close to the metal bars as possible and sealed the bone using a combination of cyanoacrylate and dental acrylic. We maintained clamping pressure as the chamber assembly was completed by bolting a top plate onto the metal bars, applying a silicone elastomer over the spinal cord, sealing the chamber with a glass coverslip on top and with additional glue around the edges, and finally gluing the skin to the base of the top plate (**Supplementary Fig. 1**, **Supplementary Protocol** and Online Methods). During 2PEF imaging, we reduced motion artifacts by securing the mouse to

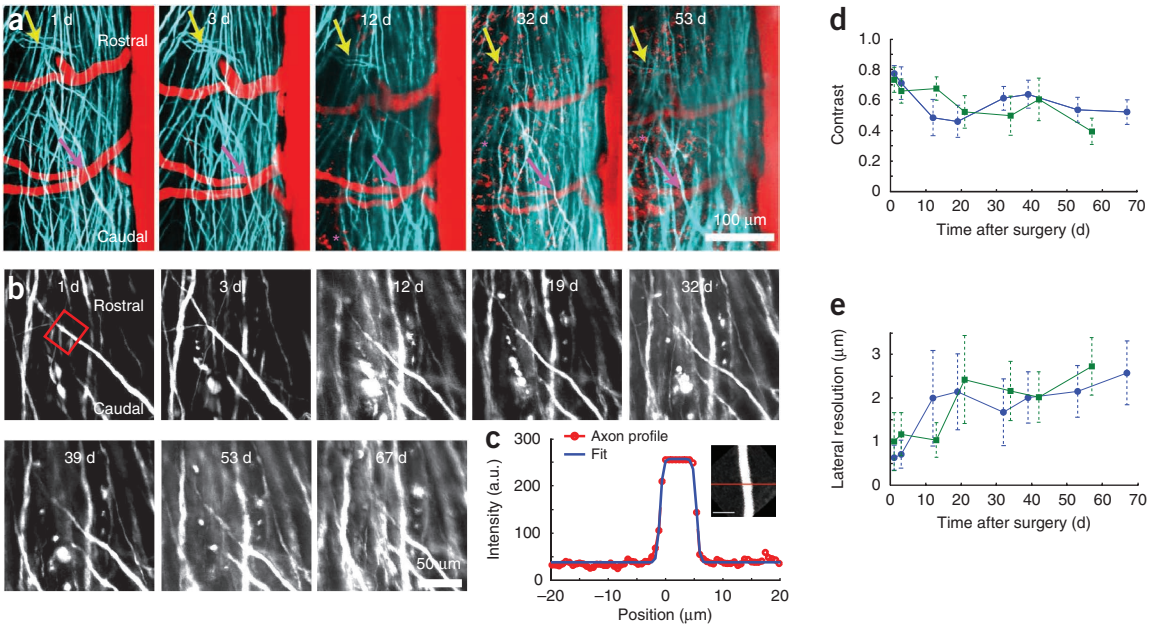

Figure 2 | Longitudinal 2PEF imaging of axons and blood vessels over many weeks after surgery. (**a**) Projections of 2PEF image stacks of afferent axons expressing EYFP (teal) and blood vessels labeled with intravenously injected Texas Red dextran (red) taken over 9 weeks after chamber implantation. Asterisks indicate the location of red autofluorescence from invading, likely inflammatory, cells located above the spinal cord at later time points. Arrows denote landmark features of the axons that were visible at all time points. (**b**) High-resolution 2PEF imaging of EYFP-expressing axons from the same region as in **a**. (**c**) Profile and fit (Online Methods, equation (3)) across maximum intensity projections of selected axon segments shown in the boxed region in **b** and in the inset; scale bar, 30 µm). A.u., arbitrary units. (**d**,**e**) Image contrast (**d**) and lateral spatial resolution (**e**) as functions of time after surgery from the fits for all axon segments for two mice (separate curves for each mouse, ~10 axons measured at each time point for each mouse). Error bars, s.d.

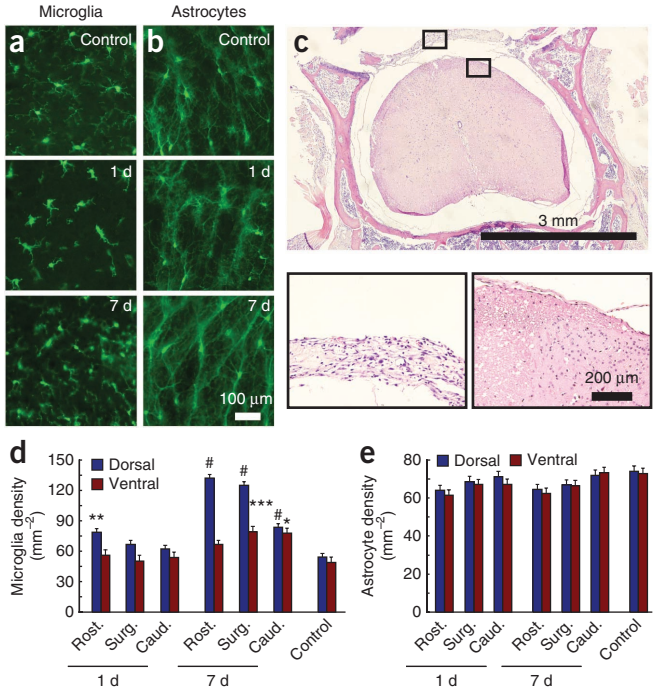

Figure 3 | Histological analysis of reactive microglia and astrocytes, and tissue morphology after chamber implantation. (**a**,**b**) Wide-field fluorescence images of 30-µm-thick coronal tissue sections from the laminectomy site 1 d and 1 week after implantation and in non-surgical controls for mice expressing EGFP in microglia (**a**) or astrocytes (**b**). (**c**) Hematoxylin and eosin–stained tissue section taken 7 d after implantation. Magnifications of the left and right boxed regions show the fibrous connective tissue that covered the dorsal aspect of the spinal cord under the implant and the neural tissue, respectively. (**d**,**e**) Microglia (**d**) and astrocyte (**e**) densites in spinal cord sections 1 and 7 d after implantation for sections one vertebra rostral to the surgical site (rost.), at the surgical site (surg.) and one vertebra caudal to the surgical site (caud.) and in controls ($^{*}P = 0.012$; $^{**}P = 0.0010$; $^{***}P = 0.0098$; $^{\#}P < 0.0001$; $n \geq 15$ measurements per segment per time point; 3 mice per time point). Error bars, s.e.m.

tapped holding posts twisted onto the set screws in the exposed wings of the top plate, thereby stabilizing the spine and elevating the mouse off of the surgical table (**Supplementary Fig. 2**) to permit free expansion of the chest cavity during inspiration. Mechanical drawings for custom parts are available in **Supplementary Notes 1–6**. The chamber enabled continuous optical access to the spinal cord (**Fig. 1c**) without repeat surgeries. Mice behaved normally over the weeks after surgery, with no signs of lordosis or kyphosis (**Fig. 1d**). Micro-computed tomography imaging of a mouse 6 d after implantation confirmed alignment of the spine and revealed no signs of vertebral damage (**Supplementary Video 1**).

Long-term imaging of spinal cord axons and blood vessels

We implanted our chamber in transgenic mice expressing enhanced YFP (EYFP) in afferent axons from a subset of DRG neurons. We imaged mice at up to eight separate times as long as 67 d postoperatively, revealing that axon morphologies and numbers of axons were stable (**Fig. 2a**). We used blood vessels labeled with Texas Red dextran and obvious features of the axons to navigate to the same region of interest across different imaging sessions. At some time points, blood vessels had increased or decreased diameter compared to baseline but with stable morphology. Image contrast visibly diminished over time, which we quantified by fitting projections of axon segments to a simple model (**Fig. 2b**,**c** and Online Methods). We found a decrease in image contrast and a loss of lateral resolution over time (**Fig. 2d**,**e**), with the greatest change occurring over the first 14 d owing to the formation of a fibrous growth over the surface of the spinal cord. The duration over which we could resolve individual axons expressing fluorescent proteins using 2PEF imaging varied between as few as 5 d and as many as 140 d (**Supplementary Fig. 3**). We found that in mice that had only minimal fibrosis 1–2 weeks after surgery, axons could routinely be resolved up to more than 5 weeks. We could image for more than 5 weeks in ~50% of the mice with implants.

At all time points, in mice in which fibrous tissue growth was minimal, imaging depth was limited to 30–50 µm by the short scattering length of myelin[19]. In cases in which fibrous growth was dense, we could not resolve axons at any depth. In some mice, we observed a myelin-poor region between adjacent dorsal roots that enabled imaging up to depths of 300 µm, well into the dorsal horn (**Supplementary Fig. 4**).

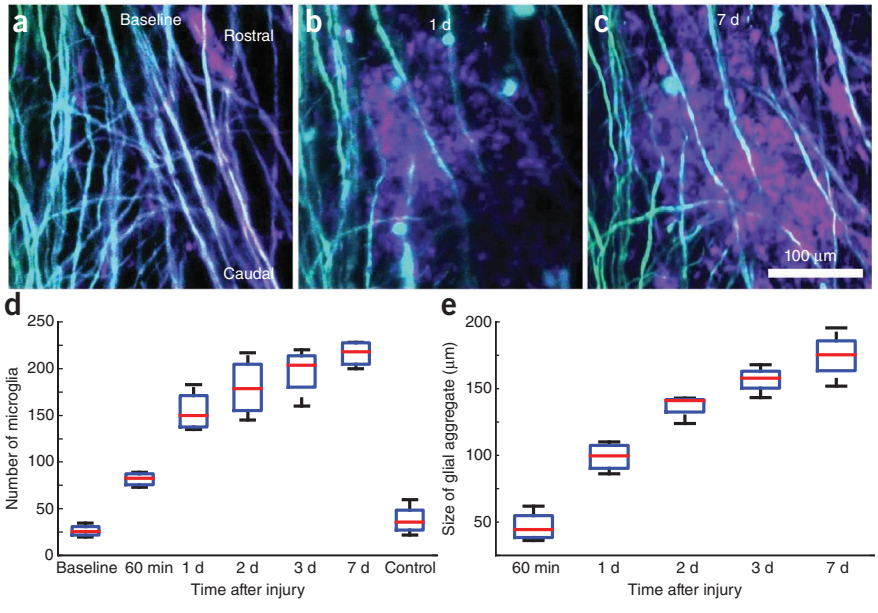

Figure 4 | Imaging and quantification of microglial scar formation at the site of a laser-induced SCI. (**a**,**b**) Projections of 2PEF image stacks of EYFP-labeled axons (teal) and EGFP-labeled microglia (mauve) before (**a**), 1 d (**b**) and 1 week (**c**) after producing a ~200-µm-long laser-induced microlesion in the spinal cord. (**d**,**e**) Boxplots of the number of microglia (**d**) and the microglial scar size (**e**) in the 300-µm field of view over time (four lesions in two mice). Horizontal red lines denote the median, blue boxes bound the 25th and 75th percentiles of the data, and the whiskers denote non-outlier extrema (defined as outside the box by less than 1.5 times the interquartile range).

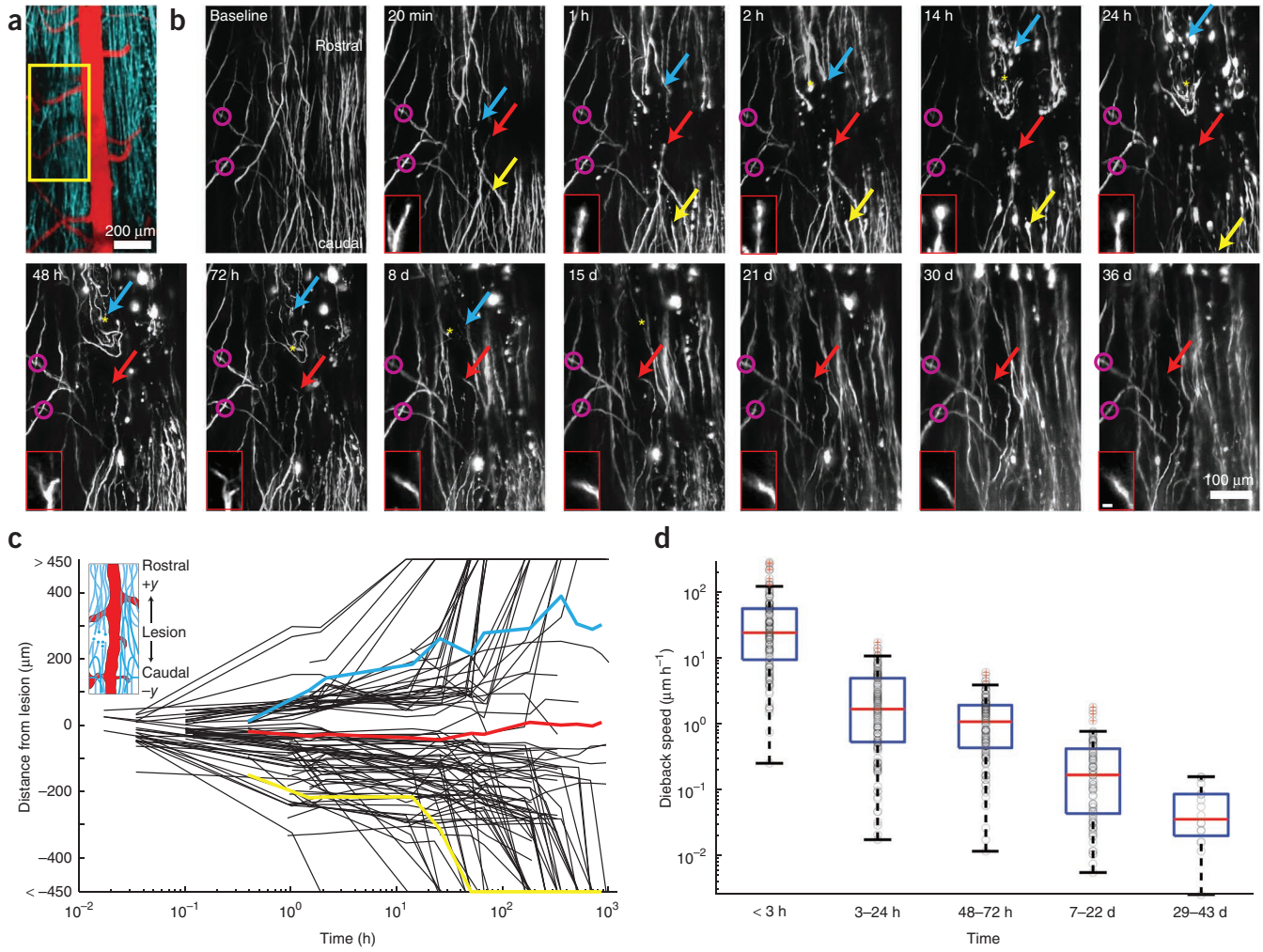

Figure 5 | 2PEF imaging and quantification of axon dieback after a laser-induced SCI. (**a**) Projection of a 2PEF image stack from mice expressing EYFP (teal) in a subset of DRG neurons with the vasculature labeled with Texas Red dextran (red). (**b**) Projections of 2PEF image stacks of EYFP-expressing axons shown in the boxed region in **a** before and at indicated times after a lesion produced by translating high-energy, tightly focused femtosecond laser pulses through the cord. Mauve circles indicate easily recognizable patterns in spared axons that were identified at all time points and provide a point of origin. Yellow arrows, axon that exhibited rapid degeneration; blue arrows, axon that died back more slowly; red arrows, axon that persisted near the lesion site and made an ultimately aborted growth response (the morphology of this axon's tip is shown in the insets; scale bar in inset, 10 µm); and *, location of early sprouting responses that did not persist over time. (**c**) Position of axon endings over time after the lesion, with positive and negative values corresponding to positions rostral and caudal to the lesion site, respectively (see schematic in inset) (107 individual axon trajectories over nine lesions in five mice). Axon trajectories in color correspond to the locations marked by respectively colored arrows in **b**. (**d**) Speed of axon-tip dieback for axons remaining in the field of view over time after the lesion. Black circles denote measurements of dieback speed from individual axon tips, horizontal red lines represent the median, the blue boxes bound the 25th to 75th percentage of the data, and the whiskers extend 1.5 times the interquartile range beyond the boxes. Points outside the whiskers were considered outliers and have a red cross through them. Because axons died back beyond the imaging field over time, the dieback speed at early times includes data from ~100 axons, and the last time point includes data for only 16 axons.

Locomotor function was preserved after implantation

We used two behavioral assays to assess the impact of the implant on motor function. We first tested mice for gait abnormalities during normal movement[20]. Mice with inked paws ran the length of a narrow enclosure, after which we analyzed the patterns of their footprints to measure base of support (lateral distance between hindlimb placement), stride length and running speed for mice with spinal chamber implants as well as sham controls (shaved and anesthetized but not receiving surgery; three mice per group). We found no remarkable differences in gait attributable to the implant at any time point (**Supplementary Fig. 5**).

In the second assay, we assessed spontaneous activity, rearing behaviors and movement speed by video-monitored open-field testing. We determined the cumulative time spent immobile, grooming, rearing and speed distributions from *post hoc* video analysis. Grooming time in mice with implants was significantly higher on days 1–3 after surgery than in sham controls, but this difference did not persist over time ($P = 0.0069$; $n = 3$ mice per group). We observed no differences in immobility or rearing times. We derived nominal top speeds from speed distributions as the average speed above the 75th percentile. Although we observed a slight reduction in top ambulatory speed in mice with implants, as compared to sham controls, it was not statistically significant (**Supplementary Fig. 5**). Finally, mice with implants did not exhibit any difficulty in grooming hindquarters or climbing (**Supplementary Video 2**).

Inflammation but no focal trauma to the spinal cord

We performed histological analysis using mice expressing EGFP in microglia (CX_3CR1-GFP) or in astrocytes (GFAP-GFP) or via standard hematoxylin and eosin staining (**Fig. 3a–c**).

We implanted the spinal chamber in the transgenic mice and perfused them for histology analysis 1 d and 1 week after surgery. We used mice that did not undergo surgery as controls (three mice per group). In mice that received implants, we analyzed sections from the site of laminectomy as well as the immediately rostral and caudal vertebrae. Both 1 d and 1 week after surgery, microglia in sections under the surgical site showed a more condensed structure with fewer processes compared to controls, but we observed no ameboid structures indicative of phagocytic microglia[21] (**Fig. 3a**). Microglia densities (**Fig. 3d**) in the dorsal aspect of the rostral segment of the spinal cord 1 d after surgery and in the dorsal aspect of all segments 1 week after surgery were elevated compared to controls. Astrocytes showed no obvious changes in morphology or cell density (**Fig. 3b**,**e**) across all groups.

For standard histopathology studies, we killed and perfused mice 1 d, 1 week and 1 month postoperatively (two mice per group). In all cases, control regions showed normal tissue in nerves, bone, muscle and spinal cord. Mild dermatitis was present at the skin-implant junction in all mice. Focal meningitis at the caudal edge of the window occurred in one mouse in the '1-week' group. We observed no signs of meningitis or disruption of neural tissue in the other mice (**Fig. 3c**) or in other regions of the mouse exhibiting focal meningitis. Neutrophils were absent in spinal cord tissue of all mice at all time points. The fibrous tissue (**Fig. 3c**) over the dorsal surface of the cord progressively thickened over time and was the limiting factor to the duration of imaging. We observed indications of muscle injury including myositis, myodegeneration and myoregeneration along with epidural neutrophilic fascitis at the site of implantation at the 1-d and 1-week time points. Reactive bone growth and fibroplasia occurred at the lateral edges of the window at the 1-month time point. The silicone elastomer showed no signs of cellular infiltration.

Numbers of microglia increased over 7 d after SCI

We used double-transgenic mice expressing EYFP in a subset of DRG axons and EGFP in microglia to evaluate the dynamics of microglial scar formation after a ~200-μm-long, 35-μm-deep laser-induced transection injury to the dorsal column produced using tightly focused femtosecond laser pulses (**Fig. 4a–c**; four lesions in two mice). We intentionally spared blood vessels in the creation of the lesion. Microglial cell counts increased dramatically during the first day and continued to increase more slowly over the following 6 d (**Fig. 4d**). The spatial extent of the densely packed microglial scar increased steadily over 7 d (**Fig. 4e**).

2PEF imaging of axon dieback after SCI

We evaluated axonal response to injury in nine laser lesions in five mice expressing EYFP in DRG afferent axons (**Fig. 5a**). We imaged two mice for 5 weeks after injury (four lesions). We collected several image stacks at the lesion site at different times after SCI (**Supplementary Video 3**). We used characteristic features of spared axons to define a common point of origin across different imaging sessions (**Fig. 5b**). We used manual tracking both from three-dimensional (3D) stacks and 2D projections to determine the distance of individual axon tips from the lesion along the rostral-caudal direction (**Fig. 5b**,**c**). Owing to axon density and insufficient spatial extent of the image stacks, we could not distinguish ascending axons from descending branches of the DRG neurons. Owing to a loss of image contrast immediately after injury, tracing was possible for most but not all axons (95 of 107 axons traced) on acute timescales (0–2 h). The average response of axons was to die back from the lesion site, but the extent and rate of axon dieback was highly heterogeneous (**Fig. 5b**,**c**). Some axons exhibited the rapid acute axonal degeneration that has been previously described[12]. Other axons persisted near the lesion site for several days or even weeks, with some mounting an abortive growth response (**Fig. 5b**,**c**). Axon tip morphology (**Fig. 5b**) also varied from day to day. The average dieback speed of the axons (defined as the change in an axon tip's axial position between successive imaging sessions divided by the elapsed time, with growth phases excluded) declined by nearly three orders of magnitude over the 5 weeks after injury (**Fig. 5d**).

DISCUSSION

Our study of microglial invasion after laser-induced SCI revealed that although the number and spatial extent of microglia continued to increase over time, the largest fractional change occurred within the first 24 h after injury, consistent with previous studies[14]. Microglia are known to phagocytose growth-inhibitory axon debris[22] in white-matter tracts[23], suggesting that the chronic, gradual recruitment of microglia may be related to the progressive degeneration of the axons involved. Thus, imaging of microglia infiltration and the clearance of axon debris will be critical for developing optimal therapeutic strategies to manipulate the microglial response.

One of the key challenges in studies of regenerative strategies for SCI is the establishment of an optimal therapeutic time window[24–27]. Although the delay of treatment has been discussed at length with respect to the glial scar[25], our observation of heterogeneity in axon dieback, instances of early but transient sprouting and decrease in dieback rate at longer timescales may suggest an optimal therapeutic window based on axon dynamics. Our axon-by-axon characterization of axon dieback rates agreed with previous studies of acute[12] and longer-term[28,29] measurements but revealed details of this transition and allowed classification of subpopulations of axons by response: ~15% were stable (remained within 400 μm of the lesion for at least 4 weeks), ~15% rapidly disintegrated (died back beyond the field of view within the first day) and ~70% progressively degenerated over the first month. Such dynamic data are inaccessible to postmortem histology or analysis of gross lesion size. In future studies we will attempt to correlate these classes of heterogeneity in axon dieback with heterogeneity in regenerative responses to therapy.

Previous studies[12,13,16,18] have demonstrated time-lapse imaging of the spinal cord via repeated surgical opening of the skin above the spinal cord. Because of the inherent stresses and risks of repeated surgeries or restrictions placed by the Institutional Animal Care and Use Committee, the number of times these procedures may be performed places severe limitations on longitudinal studies. For example, in one long-term longitudinal study, only six imaging sessions were possible in 4 months[18]. To effectively study disease dynamics and especially response to therapeutic agents, imaging must span a sufficiently long period of time to establish therapeutic limits with an imaging frequency that enables

capture of transient responses. The chamber we developed requires only a single surgery and grants continuous optical access, with the frequency of imaging being limited only by the ability of the mouse to endure multiple rounds of anesthesia. We imaged immediately after SCI up to 2 h after injury, then every 12 h for 1 d, then daily for 3 d and finally weekly for 5 weeks, for a total of 13 imaging time points after SCI.

We observed microglia at the surgical site to have higher densities and fewer processes 1 week after surgery compared to control mice, suggesting an activated but not phagocytic phenotype[21]. This result is consistent with an analogous study that considered inflammatory responses under cranial windows[30], and care will need to be taken when using our spinal cord window in studies sensitive to even mild inflammatory responses. However, we observed that even a minimal laser injury to the spinal cord results in an order of magnitude increase in microglia density near the injury, including microglia showing phagocytic ameboid morphologies. This increase far exceeds the less than twofold increase in microglia density owing to the surgery, suggesting that our chamber does not substantially confound studies in which microglial responses are more drastic.

When combined with 2PEF imaging of transgenic mice expressing fluorescent proteins in axons, microglia, astrocytes, oligodendrocytes, endothelial cells and immune cells and with nonlinear microscopy techniques to visualize myelin (for example, third harmonic generation[19]), the spinal chamber described here is an ideal tool for longitudinal studies of healthy and diseased-state spinal cord, including pathologies such as multiple sclerosis, implanted spinal cord tumors or the establishment of meningitis after bacterial challenge. As our chamber does not lead to motor deficits, functional loss or recovery may be straightforwardly correlated with cellular images.

METHODS

Methods and any associated references are available in the online version of the paper at http://www.nature.com/naturemethods/.

Note: Supplementary information is available on the Nature Methods website.

ACKNOWLEDGMENTS

We thank the US National Institutes of Health (DP OD006411 to J.R.F. and R01 EB002019 to C.B.S.) and the National Science and Research Council of Canada (to M.J.F.) for financial support, IMRA America, Inc. for the loan of their FCPA μJewel D-400 laser, J. Siebert for critically reading this manuscript, N. Ellis for his assistance in the machine shop and M. Riccio for his assistance with the MicroCT imaging.

AUTHOR CONTRIBUTIONS

M.J.F., T.A.C., J.R.F. and C.B.S. conceived and designed the experiments. M.J.F. performed surgeries and imaging experiments, I.M.B. performed behavioral assays, and D.H.S. performed histopathology. M.J.F., I.M.B., J.R.F. and C.B.S. analyzed data. J.R.F., T.A.C. and C.B.S. contributed reagents and materials. M.J.F., J.R.F. and C.B.S. wrote the paper.

COMPETING FINANCIAL INTERESTS

The authors declare no competing financial interests.

Published online at http://www.nature.com/naturemethods/.
Reprints and permissions information is available online at http://www.nature.com/reprints/index.html.

1. Kobat, D. *et al.* Deep tissue multiphoton microscopy using longer wavelength excitation. *Opt. Express* **17**, 13354–13364 (2009).
2. Christie, R.H. *et al.* Growth arrest of individual senile plaques in a model of Alzheimer's disease observed by *in vivo* multiphoton microscopy. *J. Neurosci.* **21**, 858–864 (2001).
3. Yan, P. *et al.* Characterizing the appearance and growth of amyloid plaques in APP/PS1 mice. *J. Neurosci.* **29**, 10706–10714 (2009).
4. Meyer-Luehmann, M. *et al.* Rapid appearance and local toxicity of amyloid-beta plaques in a mouse model of Alzheimer's disease. *Nature* **451**, 720–724 (2008).
5. Prada, C.M. *et al.* Antibody-mediated clearance of amyloid-beta peptide from cerebral amyloid angiopathy revealed by quantitative *in vivo* imaging. *J. Neurosci.* **27**, 1973–1980 (2007).
6. Kienast, Y. *et al.* Real-time imaging reveals the single steps of brain metastasis formation. *Nat. Med.* **16**, 116–122 (2010).
7. Lam, C.K., Yoo, T., Hiner, B., Liu, Z. & Grutzendler, J. Embolus extravasation is an alternative mechanism for cerebral microvascular recanalization. *Nature* **465**, 478–482 (2010).
8. Holtmaat, A. *et al.* Long-term, high-resolution imaging in the mouse neocortex through a chronic cranial window. *Nat. Protoc.* **4**, 1128–1144 (2009).
9. Yang, G., Pan, F., Parkhurst, C.N., Grutzendler, J. & Gan, W.B. Thinned-skull cranial window technique for long-term imaging of the cortex in live mice. *Nat. Protoc.* **5**, 201–208 (2010).
10. Drew, P.J. *et al.* Chronic optical access through a polished and reinforced thinned skull. *Nat. Methods* **7**, 981–984 (2010).
11. Bhatt, D.H., Otto, S.J., Depoister, B. & Fetcho, J.R. Cyclic AMP-induced repair of zebrafish spinal circuits. *Science* **305**, 254–258 (2004).
12. Kerschensteiner, M., Schwab, M.E., Lichtman, J.W. & Misgeld, T. *In vivo* imaging of axonal degeneration and regeneration in the injured spinal cord. *Nat. Med.* **11**, 572–577 (2005).
13. Davalos, D. *et al.* Stable *in vivo* imaging of densely populated glia, axons and blood vessels in the mouse spinal cord using two-photon microscopy. *J. Neurosci. Methods* **169**, 1–7 (2008).
14. Dibaj, P. *et al.* NO mediates microglial response to acute spinal cord injury under ATP control *in vivo*. *Glia* **58**, 1133–1144 (2010).
15. Johannssen, H.C. & Helmchen, F. *In vivo* Ca^{2+} imaging of dorsal horn neuronal populations in mouse spinal cord. *J. Physiol. (Lond.)* **588**, 3397–3402 (2010).
16. Ylera, B. *et al.* Chronically CNS-injured adult sensory neurons gain regenerative competence upon a lesion of their peripheral axon. *Curr. Biol.* **19**, 930–936 (2009).
17. Kim, J.V. *et al.* Two-photon laser scanning microscopy imaging of intact spinal cord and cerebral cortex reveals requirement for CXCR6 and neuroinflammation in immune cell infiltration of cortical injury sites. *J. Immunol. Methods* **352**, 89–100 (2010).
18. Dray, C., Rougon, G. & Debarbieux, F. Quantitative analysis by *in vivo* imaging of the dynamics of vascular and axonal networks in injured mouse spinal cord. *Proc. Natl. Acad. Sci. USA* **106**, 9459–9464 (2009).
19. Farrar, M.J., Wise, F.W., Fetcho, J.R. & Schaffer, C.B. *In vivo* imaging of myelin in the vertebrate central nervous system using third harmonic generation microscopy. *Biophys. J.* **100**, 1362–1371 (2011).
20. Crawley, J.N. *What's Wrong with My Mouse? Behavioral Phenotyping of Transgenic and Knockout Mice* (Wiley-Liss, New York, 2000).
21. Streit, W.J., Walter, S.A. & Pennell, N.A. Reactive microgliosis. *Prog. Neurobiol.* **57**, 563–581 (1999).
22. Tanaka, T., Ueno, M. & Yamashita, T. Engulfment of axon debris by microglia requires p38 MAPK activity. *J. Biol. Chem.* **284**, 21626–21636 (2009).
23. Aldskogius, H. & Kozlova, E.N. Central neuron-glial and glial-glial interactions following axon injury. *Prog. Neurobiol.* **55**, 1–26 (1998).
24. Garcia-Alias, G. *et al.* Therapeutic time window for the application of chondroitinase ABC after spinal cord injury. *Exp. Neurol.* **210**, 331–338 (2008).
25. Rolls, A., Shechter, R. & Schwartz, M. The bright side of the glial scar in CNS repair. *Nat. Rev. Neurosci.* **10**, 235–241 (2009).
26. Tator, C.H. Review of treatment trials in human spinal cord injury: issues, difficulties, and recommendations. *Neurosurgery* **59**, 957–987 (2006).
27. Thuret, S., Moon, L.D. & Gage, F.H. Therapeutic interventions after spinal cord injury. *Nat. Rev. Neurosci.* **7**, 628–643 (2006).
28. Seif, G.I., Nomura, H. & Tator, C.H. Retrograde axonal degeneration ("dieback") in the corticospinal tract after transection injury of the rat spinal cord: a confocal microscopy study. *J. Neurotrauma* **24**, 1513–1528 (2007).
29. Silver, J., Horn, K.P., Busch, S.A., Hawthorne, A.L. & van Rooijen, N. Another barrier to regeneration in the CNS: activated macrophages induce extensive retraction of dystrophic axons through direct physical interactions. *J. Neurosci.* **28**, 9330–9341 (2008).
30. Xu, H.T., Pan, F., Yang, G. & Gan, W.B. Choice of cranial window type for *in vivo* imaging affects dendritic spine turnover in the cortex. *Nat. Neurosci.* **10**, 549–551 (2007).

ONLINE METHODS

Surgical procedure. We anesthetized mice under 5% isoflurane on a custom-built surgery table (**Supplementary Fig. 2**) and then maintained on ~1.5% isoflurane in 100% oxygen. We injected 0.05 mg of glycopyrrolate (an anticholinergic) per 100-g mouse intramuscularly. We also injected 1 ml per 100-g mouse of 5% (w/v) glucose in normal saline subcutaneously hourly. We used a rectal thermometer and feedback-controlled heating blanket to maintain body temperature at 37.5 °C. We shaved the dorsal surface above the thoracic spine and applied three alternating washes each of 70% (v/v) ethanol and iodine to the skin to reduce the likelihood of infection. We gave a subcutaneous injection of 0.1 ml of 0.125% (v/v) bupivicaine at the site of skin incision.

We made a small incision in the skin at the T11–T13 level of the mouse's spine and held back the skin with retractors. We made an incision three vertebrae long on either side of T12 and scraped the bone clean on the top and the sides. We severed tendons attached to the three vertebrae using surgical scissors. We trimmed all incongruous tissue to reduce necrosis. We used sterile cotton applicators to control bleeding. We clamped the three vertebrae by magnetic stainless steel bars with a notched groove and held under pressure on 30-mm stainless steel posts with a three-pronged plug, consisting of two pins to prevent rotation and a central magnet to hold the bar. We removed the dorsal lamina of T12 using vanna scissors, and used sterile gel foam (Pharmacia & Upjohn Co.) or cotton applicators along with sterile saline to control bleeding and keep blood off the surface of the cord. We trimmed the lateral edges of the bone back as close as possible to the edges of the bars and the surface of the bone sealed with dental acrylic and cyanoacrylate. Where possible, we left the dura intact.

Keeping the cord irrigated with normal saline, we positioned a top plate and screws inserted into the metal bars. We injected Kwik-Sil silicone elastomer (World Precision Instruments) into the space between the cord and the top plate and sealed the chamber with a 5-mm diameter coverslip. We used cyanoacrylate glue and dental acrylic to seal the chamber at the rostral and caudal vertebrae. With pressure maintained by the screws, we removed the three-pronged steel posts. We pulled the skin to the edge of the implant and secured it with cyanoacrylate glue and dental acrylic. We inserted set screws into the wings of the top plate. An illustration of the procedure with accompanying photographs is available in **Supplementary Figure 1**. We again injected bupivicaine (0.1 ml, 0.125%) around the edge of the implant. During recovery, we placed the mouse on a heated surface and administered ketoprofen (5 mg kg^{-1} d^{-1}) and dexamethasone (0.2 mg kg^{-1} d^{-1}) every 24 h for 72 h. A step-by-step description of how to perform the procedure, with suggested solutions to common problems, is available in the **Supplementary Protocol**. We performed all surgery under a stereomicroscope (Leica MZ12.5).

All animal procedures performed were approved by the Cornell Institutional Animal Care and Use Committee and were performed under the guidance of the Cornell Center for Animal Resources and Education.

Mice. For imaging, we used mice of the YFP-H line (Jackson Labs), which express EYFP in a subset of pyramidal neurons and dorsal root ganglia. In addition we used CX_3CR1-GFP mice (Jackson Labs), which express EGFP in microglia. We also used crosses between the YFP-H and CX_3CR1-GFP lines.

For histopathological analysis, we used mice of the YFP-H line and mice of the Emx-1-cre (Jackson Labs) lines. We used CX_3CR1-GFP mice and GFAP-GFP (Jackson labs), which express GFP in astrocytes, to study reactive gliosis in microglia and astrocytes, respectively.

In all cases, mice were of both sexes and 3–12 months in age when the device was implanted, and they were heterozygous for each transgene. Mice were group-housed before chamber implantation and were singly housed in rat-size cages after implantation to minimize the risk of the mouse bumping the implanted chamber against the cage lid.

Histology. We deeply anesthetized mice and perfused them transcardially with phosphate buffered saline (PBS; pH 7.4) (Sigma-Aldrich) to clear the blood, followed by fixation with 4% (w/v) paraformaldehyde (PFA) (ThermoFisher Scientific) in PBS.

For gliosis studies in GFAP-GFP and CX_3CR1-GFP mice, we immersed whole spines in PFA for 1 d after perfusion followed by removal of the spinal cord from the vertebral canal by microsurgical dissection. We immersed dissected spinal cords in 30% (w/v) sucrose in PBS until saturated. We froze spinal cords in optimal cutting temperature (OCT) compound (Tissue-Tek) and cut sections at a nominal thickness of 30 µm on a Microm HM550 cryotome (ThermoFisher Scientific). We took sections at the rostral and caudal edges of the implant, under the glass and control regions located one vertebrae in the rostral and caudal direction from the edges of the implant. We examined tissues under an Olympus BX41 wide-field fluorescence microscope.

For hematoxylin and eosin staining–based histopathology studies, we examined whole fixed mice for gross pathology, and gently freed and removed the skin surrounding the chambers. We separated the chambers from their attachment to the subjacent vertebral bodies starting at one end by gentle dorsal traction. Once freed from the vertebral bodies, we carefully separated the chambers from subjacent soft tissues (epaxial muscle and connective tissues). We removed any material (mostly injected silicone) that had adhered to the ventral surface of the glass windows using a scalpel and reserved it for staining. After removing ribs and organs from the vertebral column, we collected 3-mm cross-sections of the vertebral column, including surrounding muscle, from ~1 cm rostral, 1 cm caudal and directly below the center of the window by making cuts perpendicular to the vertebral column using a broad tissue blade. We inserted tissues into cassettes and immersed them again in PFA. We decalcified tissues by rinsing tissue cassettes under running water for 15 min, followed by placement in a vacuum jar containing equal volumes of 20% (w/v) sodium citrate dihydrate and 50% (v/v) formic acid. Tissues were held under vacuum at room temperature (20–25 °C) with constant stirring using a magnet for ~24 h. After this procedure, we rinsed tissues under running water for 10 min and put in a solution of 70% (v/v) ethyl alcohol. We then embedded tissues in paraffin wax using an automated tissue processor (Tissue-Tek VIP), sectioned (4-µm thick sections) them and stained them with hematoxylin and eosin using an automated stainer (Shandon Varistain 24-4; Thermo Scientific). We sealed slides with a coverslip and examined them using an Olympus BX40 microscope.

2PEF microscopy. To image (or reimage) the spinal cord, we anesthetized mice with isoflurane and placed them on the custom

surgery table described previously for the laminectomy procedure. Mice also received glycopyrrolate and glucose as described above. We used tapped 30-mm posts secured in an optical post holder to screw finger-tight onto the set screws of the wings of the top plate of the implant to locally immobilize the spine (**Supplementary Fig. 1g**). We elevated mice slightly by the implant to allow room for chest expansion and contraction during breathing. After imaging, we twisted off the posts and the mouse was allowed to recover on a heated surface.

We performed imaging using a custom-designed multiphoton microscope with a 20× water-immersion objective lens (numerical aperture (NA) = 1.0; Carl Zeiss MicroImaging), a 40× water-immersion objective (NA = 0.8; Olympus) or a 4× objective (NA = 0.28; Olympus). We performed 2PEF imaging using 1,043-nm wavelength, 1-MHz, 300-fs pulses from a fiber laser (FCPA μJewel D-400; IMRA) and/or 920-nm, 87-MHz, 100-fs pulses from a Ti:sapphire laser oscillator (MIRA HP; Coherent). We used emission filters at 645/65 nm (center wavelength/bandwidth), 550/50 nm and 517/65 nm (Chroma Technology) to isolate fluorescence from Texas Red dextran, YFP and GFP, respectively (see **Supplementary Note 7** for individual image details).

Spinal cord lesioning. We made lesions measuring 100–300 μm long, 5–10 μm wide and 30–40 μm deep in the dorsal spinal cord by femtosecond laser ablation using ~100-nJ pulses from a regenerative amplifier (800-nm wavelength, 50-fs pulse duration, 1-kHz repetition rate; Legend, Coherent). We used custom software in Matlab (MathWorks) to define a 2D trajectory by tracing a pattern on a *z*-dimension projection of a 3D image stack. To minimize the loss of image contrast caused by excessive bleeding, we intentionally avoided cutting blood vessels where possible. To execute the pattern, the mouse was translated at 500 μm s^{-1} along the traced trajectory in the *x*-*y* plane while a shutter controlling the femtosecond pulses was opened, producing a cut ~2–3 μm deep. The mouse was then translated by 1 μm in the *z* direction, and the cut pattern was repeated. This procedure was iterated until a cut depth of 30–40 μm was achieved. The shutter was closed during translation in the *z* dimension. When deemed necessary, we repeated the cut to ensure complete transection of axons. Because the damage was mediated by an electron-ion plasma formed by nonlinear optical absorption and there was very little thermal energy deposited, the damage was largely confined to the focal volume.

Image processing. We computed image projections by taking the s.d. along the *z* axis of three-dimensional image stacks. For contrast and resolution measurements, we used maximum pixel intensity projections of isolated axon segments. As we oversampled image stacks, we manually removed frames with large motion artifacts resulting from breathing without loss of information. Owing to the high density of microglia observed after SCI, there was ambiguity in distinguishing cell bodies from densely packed processes. We manually identified microglia cell bodies as fluorescent ameboid structures with visible boundaries, traced them and counted them in 2D projections using custom Matlab software. We defined microglia scar size as the mean square radius in manual traces of the boundary of the largest contiguous aggregate of microglia. For axon tracing, we Fourier filtered high-resolution (0.59 μm $pixel^{-1}$) 3D image stacks, took the s.d. projection and stitched the images together using PanaVue stitching software. We used spared axons that were stable over the duration of the experiments to define a common point of origin among imaging sessions. We marked axon endings and tracked them using custom software in Matlab. We resolved ambiguities by examining trajectories in the 3D stacks.

In double-transgenic mice expressing YFP in axons and GFP in microglia, we used emission filters with 517/65 nm and 550/50 nm (center wavelength/bandwidth) with 920-nm excitation for 2PEF imaging. We linearly unmixed images in custom software written in Matlab. Briefly, we manually selected image features corresponding to axons (YFP) or microglia (GFP) in both imaging channels and generated a mixing matrix. We then solved for the inverse matrix and calculated the resultant unmixed images containing separate fluorescent species.

Contrast and resolution fitting. To characterize the contrast and resolution, we first used ImageJ to isolate axon segments of ~40–50 μm in length from image stacks the same region across multiple days. We performed subsequent analysis in Matlab. We computed the maximum projection along the *z* axis and median-filtered the resulting image with a 1-pixel filter radius. To orient the segment so that the axis ran parallel to the *y* axis, we used a radon transform to find the angle of orientation and rotated the image accordingly.

As we considered the maximum intensity projection across the axon volume, the intensity profile is equal to the value of the intensity profile taken immediately through the center of the axon, where, to good approximation, the excited fluorescence in the axon is approximately constant in the *x* direction. For an axon of radius *R*, and displaced from the origin by an amount δ, the fluorophore concentration profile, *C*, in a single scan at the center is

$$C(x) = C_0\left(\theta(x+R+\delta) - \theta(x-R+\delta)\right) \tag{1}$$

where C_0 is the axonal fluorophore concentration and $\theta(x)$ is the Heaviside step function. For a Gaussian excitation beam with intensity profile

$$I(x) = I_0 \exp\left(-\frac{x^2}{2a^2}\right) \tag{2}$$

where I_0 is the peak laser intensity and *a* is a measure of the beam waist. The image intensity, $F(x)$, is given by the convolution of equations (1) and (2) with the addition of a background noise floor, *B*

$$F(x) = A\left(\operatorname{erf}\left(\frac{x+R+\delta}{\sqrt{2}a}\right) - \operatorname{erf}\left(\frac{x-R+\delta}{\sqrt{2}a}\right)\right) + B \tag{3}$$

where

$$A = \sqrt{\frac{\pi}{2}} a I_0 C_0 \tag{4}$$

We fit equations (3) to each line of the axon profile (**Fig. 2c**) and averaged the results. Failure to converge by nonlinear

doi:10.1038/nmeth.1856

least-squares fitting or an R^2 value less than 0.85 was used to exclude data points. We defined contrast as

$$\frac{F(-\delta) - B}{F(-\delta) + B}, \quad (5)$$

which ranges between 0 (no contrast) and 1 (noiseless contrast), where $F(-\delta)$ is the intensity peak in the axon. We took resolution as the parameter a.

Behavioral assays. We subjected mice to open-field and runway assays. We first made measurements 1 d before implantation of an imaging window, followed by measurements each day for the first 7 d and a final time point at 14 d after implantation. We made all measurements at the same time of day to avoid circadian variability. We tested mice that were shaved and anesthetized, but not operated on, simultaneously as sham controls.

We constructed analysis of footprints from the runway assay in which mice with inked paws traversed the length of a Plexiglass enclosure (76 cm long × 8 cm wide × 20 cm high) to enter a dark goal box at the end of the runway. We placed mice on an inked pad in a 15-cm-long staging area separated from the main runway by a sliding insert. We placed paper tape on the floor of the runway to collect ink pawprints. Removal of the insert marked the beginning of the trial. All trials were video-recorded from above. We performed three trials at each time point, and took footprint measurements from 5 consecutive steps in each trial. We then returned mice to their home cage between trials to minimize the effects of fatigue. Mice received 10–14 d of behavioral training before surgery. During training, we encouraged mice to traverse the length of the runway without pausing, receiving prompting from the experimenter where necessary. We deemed training complete when mice traversed the length of the runway without pausing or prompting. We assessed hindlimb base of support as the lateral distance between hindlimbs and stride length as the distance between the central pads of two consecutive hindlimb prints on the left or right. We determined average speed by dividing the runway length by the total time of the trial, as determined by the video clock.

We assessed rearing, grooming, mobility and top ambulatory speeds in open-field measurements. We placed mice in the center of a Plexiglass enclosure (46 cm long × 46 cm wide × 47 cm high) with black sides and a white base. We recorded mice from above for 5 min under red-light illumination. Video tracking analysis was performed based on the videos using ANY-maze software (Stoelting Company) and Matlab. We defined rearing as any period during which the mouse lifted both of its forelimbs off the ground simultaneously. We defined grooming as any period during which the animal licked its fur or moved its forelimbs over the head. Top speeds were determined as the mean of the speeds greater than the 75th percentile.

Statistical analysis. We compared grooming time, time spent immobile, rearing time, base of support, stride length and average speed using the analysis of variance (ANOVA) test. Where the null hypothesis was rejected, we performed *post hoc* analyses using Tukey's honestly significant difference for pairwise comparisons. We compared top speeds of mice receiving surgery and sham treatments each day using a Mann-Whitney U test.

We compared microglia and astrocyte densities using ANOVA. Where the null hypothesis was rejected, we performed *post hoc* analyses using Tukey's honestly significant difference on mean to compare groups.

We performed statistical tests in Kaelidograph (Synergy) and Matlab. We set the criterion for significance in all cases to be $\alpha = 0.05$.

Nature Methods

Chronic *in vivo* imaging in the mouse spinal cord using an implanted chamber

Matthew J Farrar, Ida M Bernstein, Donald H Schlafer, Thomas A Cleland, Joseph R Fetcho &

Chris B Schaffer

Supplementary Figure 1	A metallic spinal chamber implant was mounted via a custom delivery system onto the vertebral column and provided long-term optical access to the spinal cord.
Supplementary Figure 2	A custom surgery table allows for both surgery and imaging procedures
Supplementary Figure 3	Imaging with individual axonal resolution is possible out to as many as 140 days post-surgery
Supplementary Figure 4	Anatomically myelin-poor regions of the spinal cord enable deep- tissue imaging
Supplementary Figure 5	Implanted mice do not show significant changes in mobility or motor function compared to sham controls
Supplementary Note 1	Mechanical drawing: chamber top plate
Supplementary Note 2	Mechanical drawing: chamber side bars
Supplementary Note 3	Mechanical drawing: surgical table front/back
Supplementary Note 4	Mechanical drawing: surgical table center
Supplementary Note 5	Mechanical drawing: chamber holder for imaging
Supplementary Note 6	Mechanical drawing: bar holder for surgery
Supplementary Note 7	Equipment and settings
Supplementary Protocol	Detailed step-by-step surgical protocol and troubleshooting guide

Note: Supplementary Videos 1–3 are available on the Nature Methods website.

Supplementary Figure 1

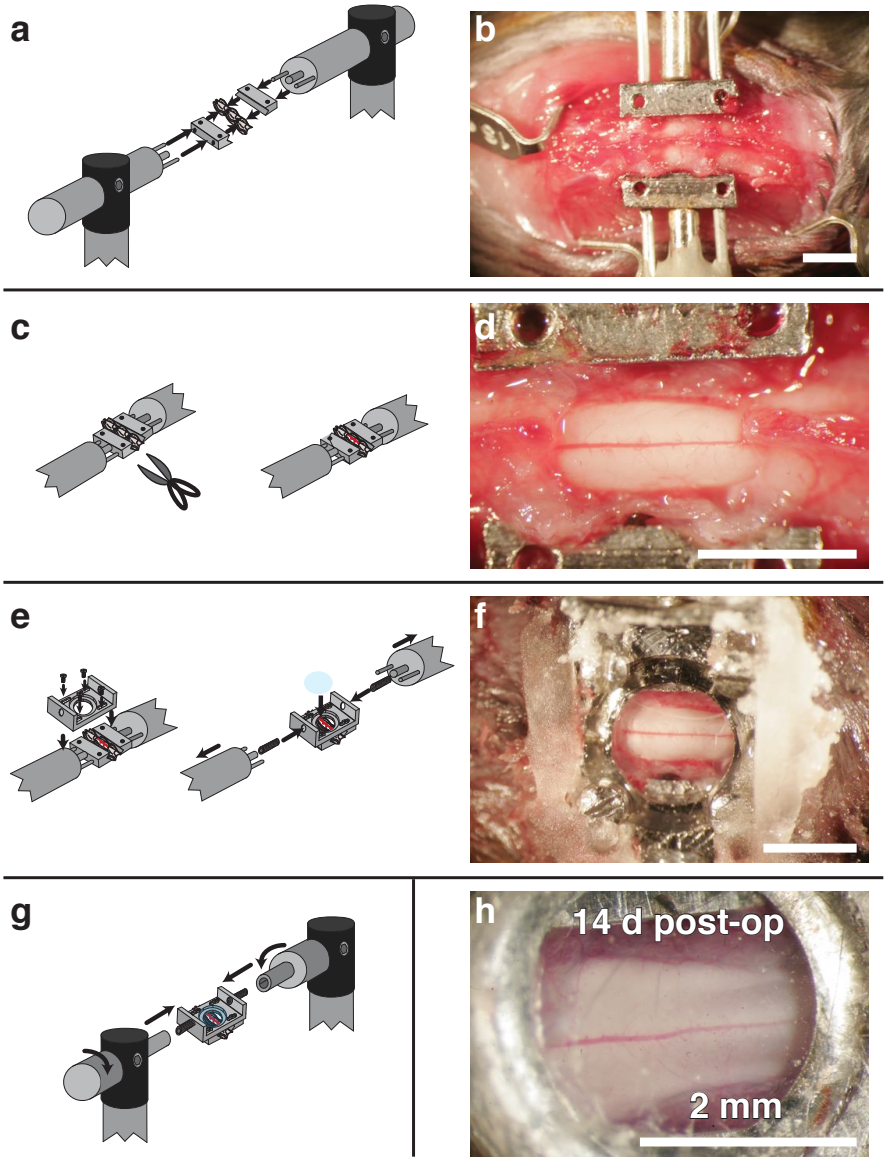

Supplementary Figure 1: A metallic spinal chamber implant was mounted via a custom delivery system onto the vertebral column and provided long-term optical access to the spinal cord. The exposed vertebrae (T10-T12) were clamped by notched metal bars attached to holder posts (**a**,**b**) after soft muscle had been retracted. Vanna scissors were used to complete a dorsal laminectomy (**c**,**d**) on the central vertebra (T11). A top plate was secured using four screws, maintaining the clamping pressure (**e**). Silicone elastomer was placed over the cord and the chamber was sealed with glass, while set screws were inserted into the wings of the top plate (**e**,**f**). Holder posts were removed (**e**) and the skin was sealed using a combination of cyanoacrylate adhesive and dental acrylic cement (**f**). To image, mice were anesthetized and the spine was locally immobilized by securing the implant to holder posts via the set screws (**g**). Optical access was possible for several weeks or more (**h**).

Supplementary Figure 2

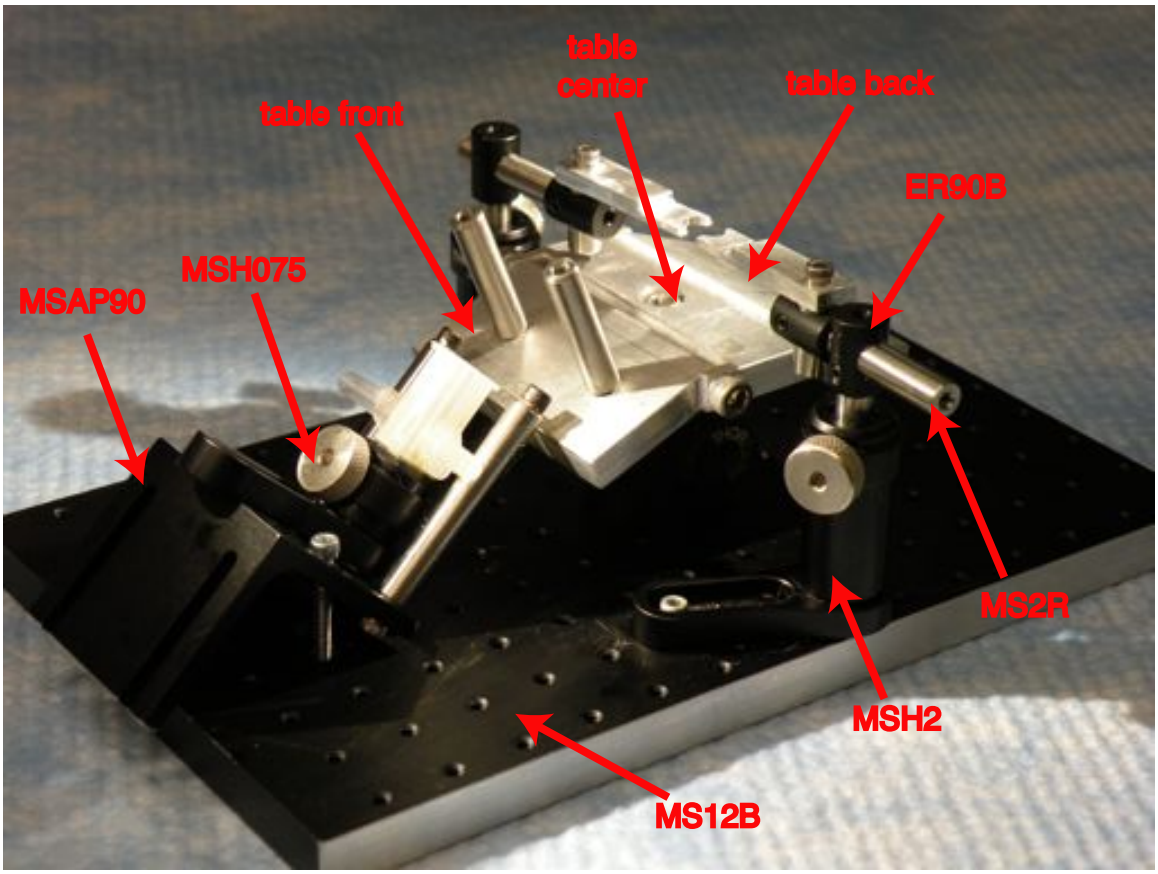

Supplementary Figure 2: A custom surgery table allows for both surgery and imaging procedures. A procedure table –composed of rotary wings and a center part–designed for surgery and imaging is readily built with relatively inexpensive optics parts. Parts as labeled are available from Thor Labs under the following part numbers: ∅6 mm posts (MS2R) and post-holders (MSH2), right-angle post adapters (ER90B), post-holder for nose-cone (MSH075), angle bracket (MSAP90), ∅1/2" post (TR2) and post-holder (PH1.5) (below the surgery table), and breadboard (MS12B). The posts that screw to the set screws in the top plate of the imaging chamber, as illustrated in Fig. 1g, mount to the ER90B right-angle adaptors. Shown mounted here is a vertebral clamp for acute imaging where a chronic chamber is not required. Optionally, posts can be added to the table front to prevent sliding during surgery.

Supplementary Figure 3

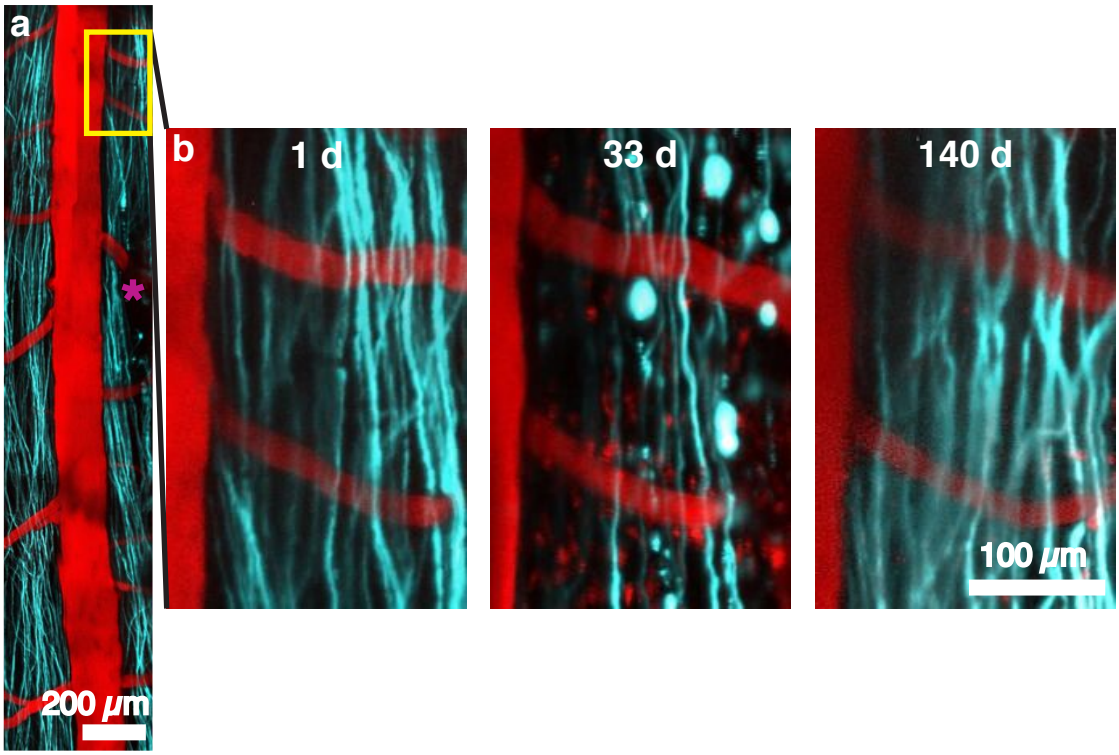

Supplementary Figure 3: Imaging with individual axonal resolution is possible out to as many as 140 days post-surgery. In one animal considered, multiple imaging sessions were possible out to as long as 140 days. An injury induced during surgery was evident one day after the surgery (**a**, mauve asterisk) and a region rostral to the injury (**a**, yellow box) remained sufficiently clear so as to image individual axons. Axonal degeneration progressed rostrally over time (**b**), with little change on one day post-surgery, severe degeneration in the selected region by day 33, and only spared axons present at day 140.

Supplementary Figure 4

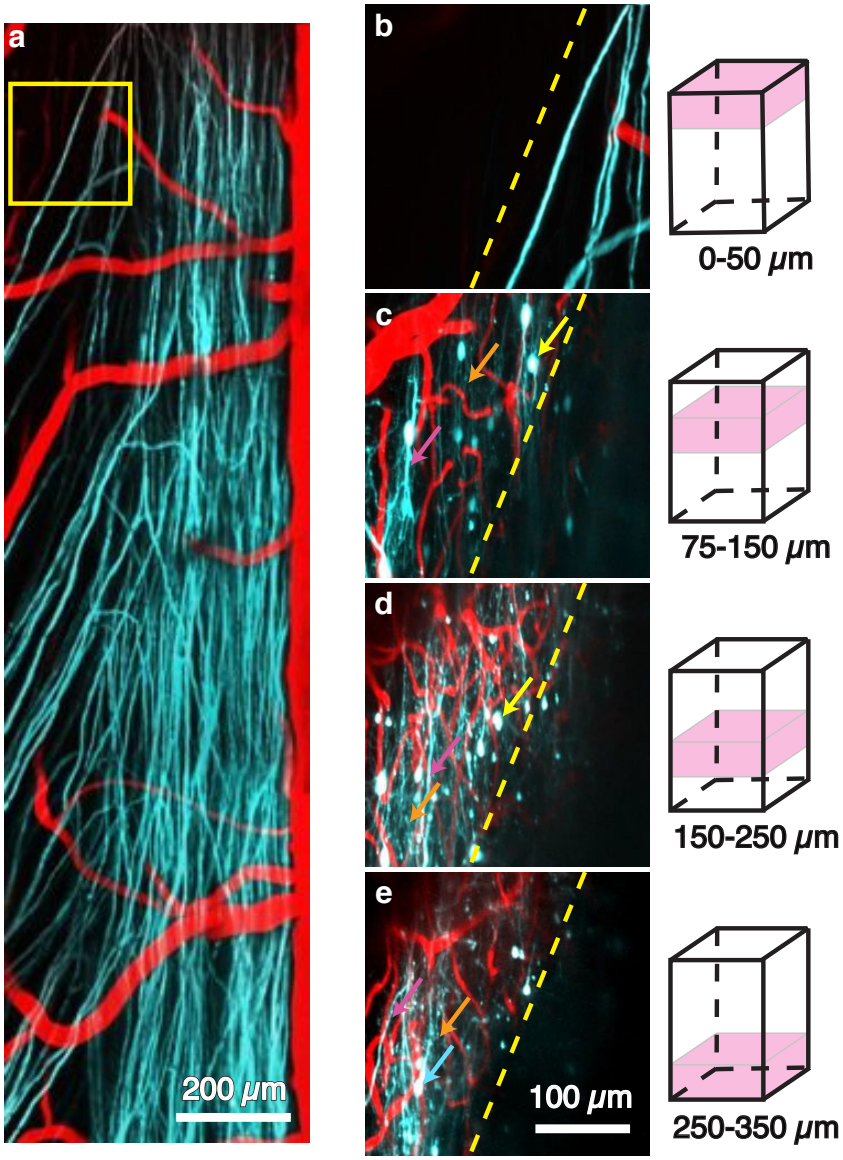

Supplementary Figure 4: Anatomically myelin-poor regions of the spinal cord enable deep-tissue imaging. Regions of the dorsolateral spinal cord between dorsal roots (**a**, yellow box) exhibit regions deficient of densely myelinated axons (YFP, teal). In these regions, imaging of neuron cell bodies (yellow arrows), dendrites (orange arrows), axons (mauve arrows), and vasculature (Texas Red dextran, red) in the dorsal horn is possible up to several hundred micrometers below the surface (**b**-**e**). Image projections are taken at and over the depths given by the illustrations (right). The dotted line marks the stark change in contrast between areas underlying myelinated superficial axons and regions of sparse axon density.

Nature Methods: doi:10.1038/nmeth.1856

Supplementary Figure 5

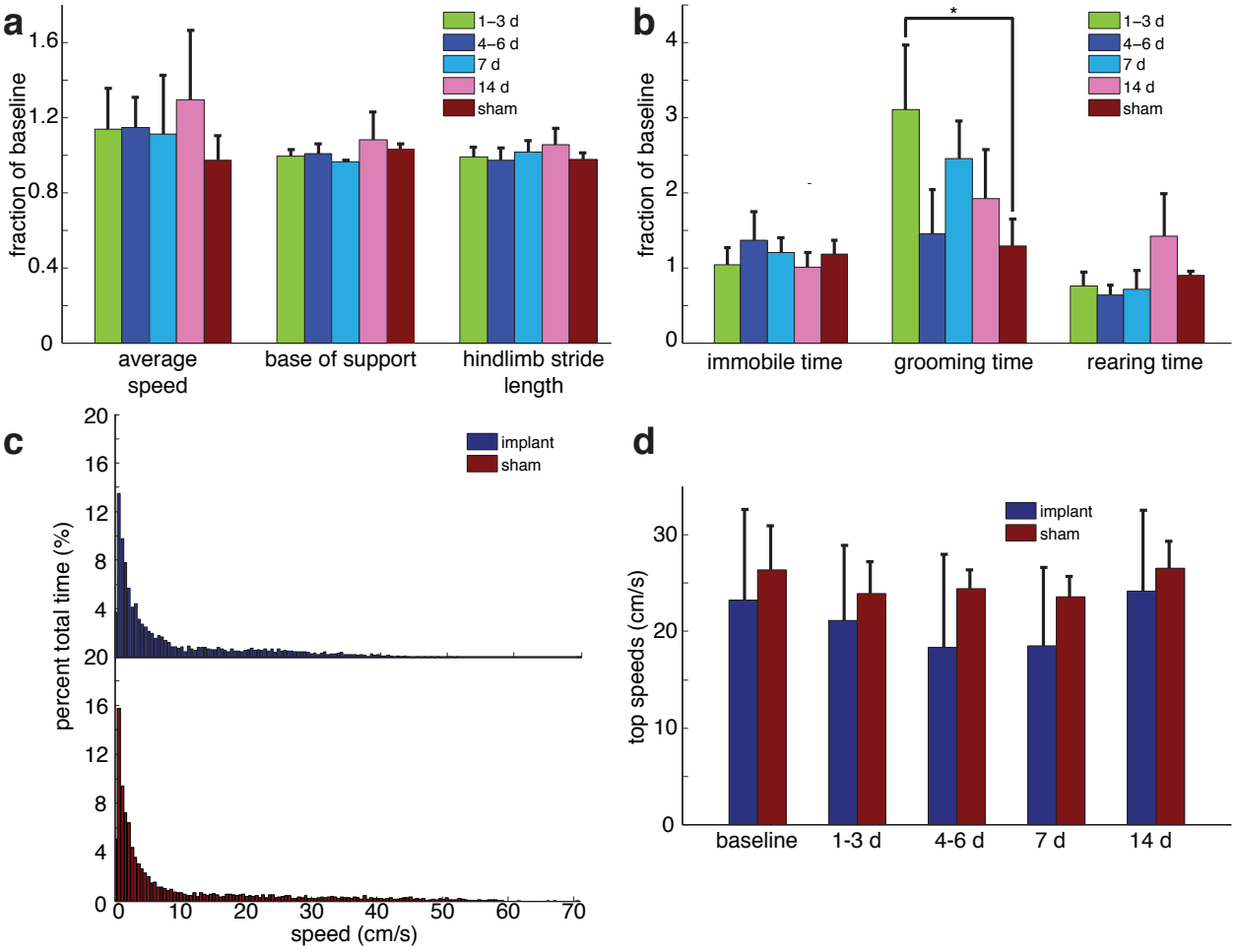

Supplementary Figure 5: Implanted mice do not show significant changes in mobility or motor function compared to sham controls. Measurements of ink footprints and videography of implanted and control mice running down an enclosed track were used to determine stride length, base of support, and average speed. Measurements were taken from multiple post-operative timepoints as well as from sham-operated controls (n = 3 mice per group; consecutive daily measurements made in each group), with results expressed as a fraction of the preoperative within-subject baseline (a). No significant differences were seen between groups in any category. Open field testing also was used to measure cumulative rearing time, grooming time, and time spent immobile during a 5-minute test. Grooming time was significantly higher in implanted mice 1-3 days post-operatively than in controls (P = 0.0069; n = 3 mice per group); otherwise, implanted mice did not differ from controls (b). Top speed was characterized from the speed histogram (c) as the mean of the speeds above the 75th percentile. Top speeds were compared both pre-operatively and post-operatively (d) and no significant differences were seen across groups. Error bars denote the standard deviation.

Supplementary Note 1

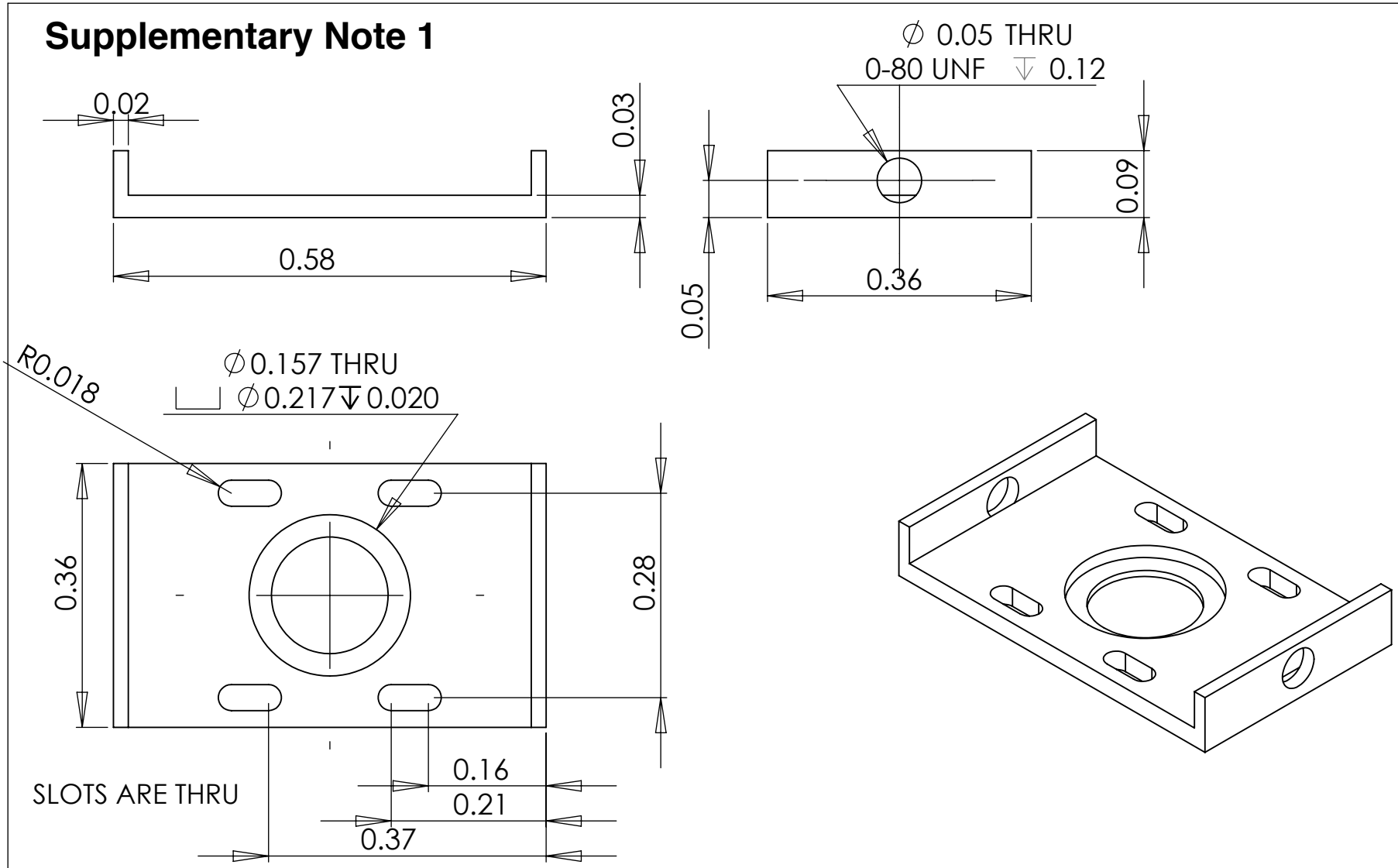

SCALE 5:1

PART: CHAMBER TOP PLATE
QUANTITY: 1
MATERIAL: 316 STAINLESS STEEL

Nature Methods: doi:10.1038/nmeth.1856

Supplementary Note 2

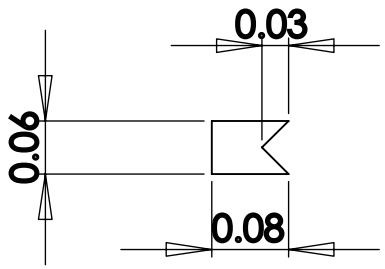

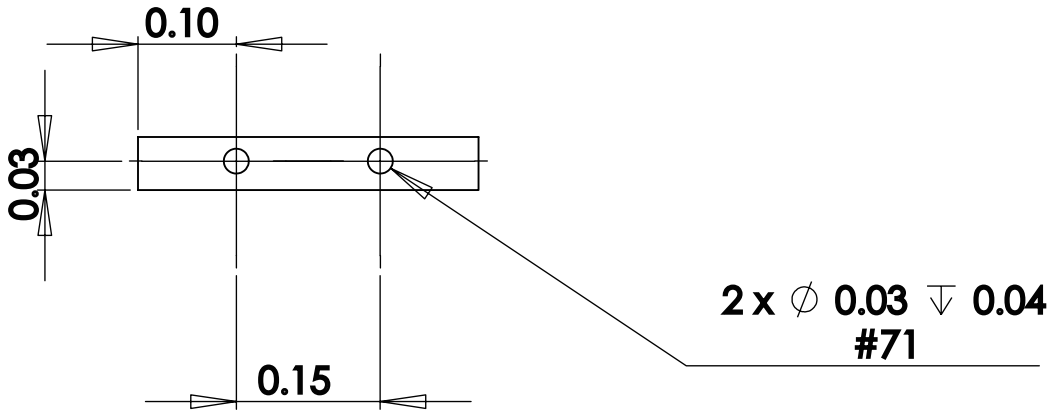

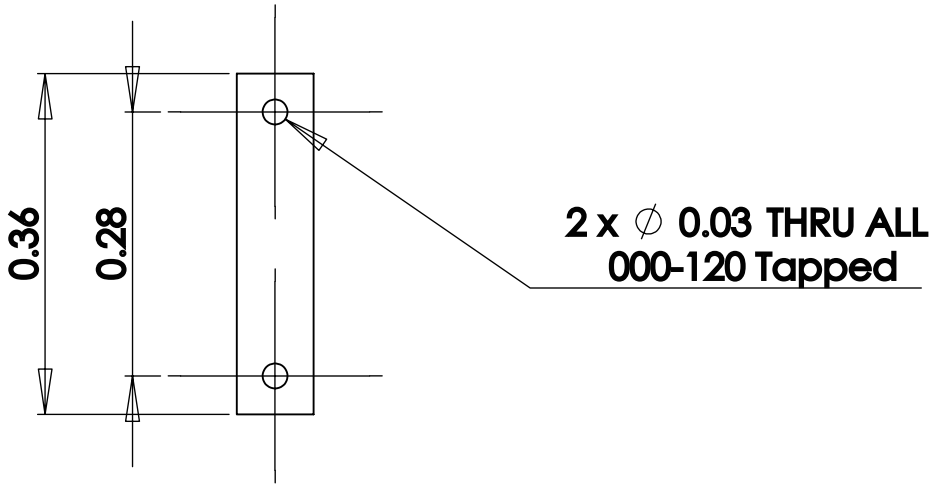

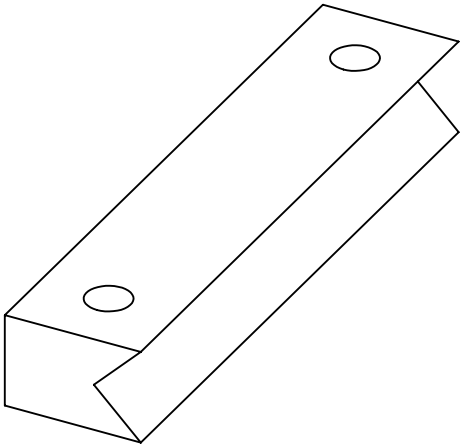

SCALE: 5:1

PART: CHAMBER SIDE BAR
QUANTITY: 2
MATERIAL: MAGNETIC STAINLESS STEEL (E.G. 430)

Nature Methods: doi:10.1038/nmeth.1856

Supplementary Note 3

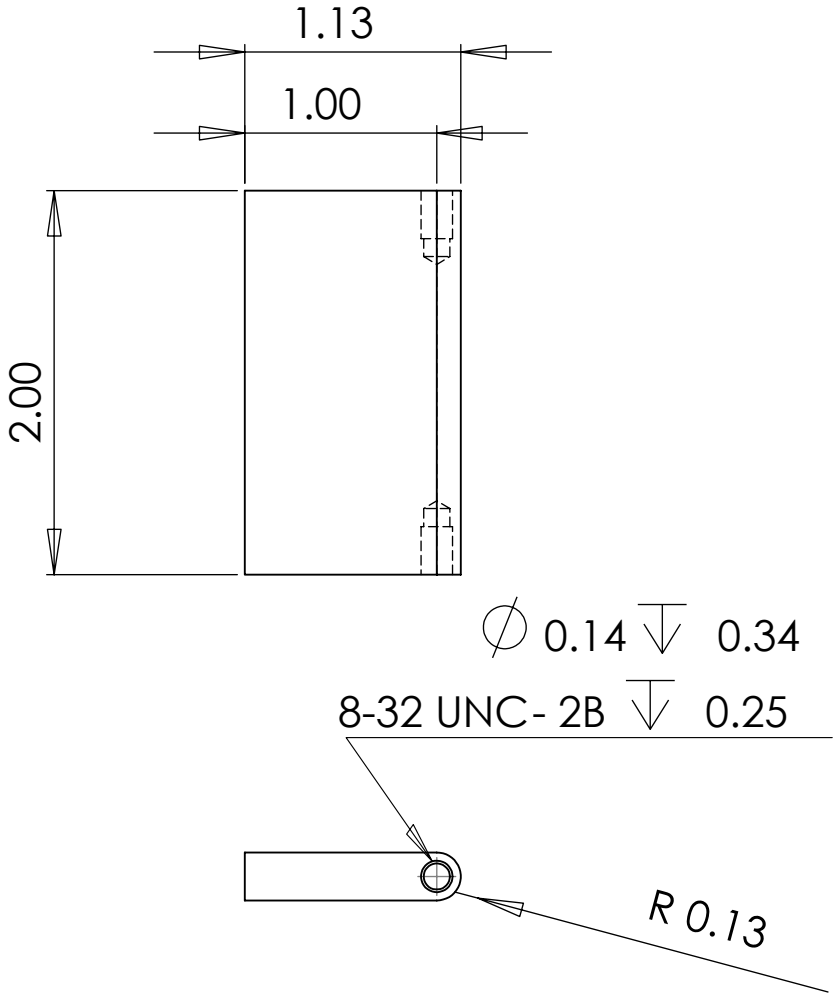

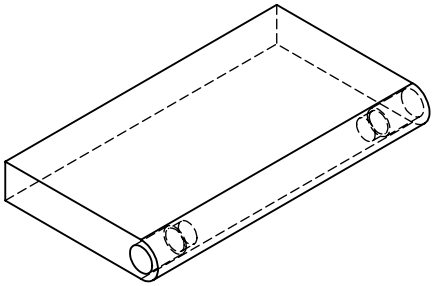

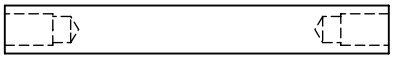

SCALE: 1:1

PART: TABLE FRONT/BACK
QUANTITY: 2
MATERIAL: ALUMINUM

REV

Nature Methods: doi:10.1038/nmeth.1856

Supplementary Note 4

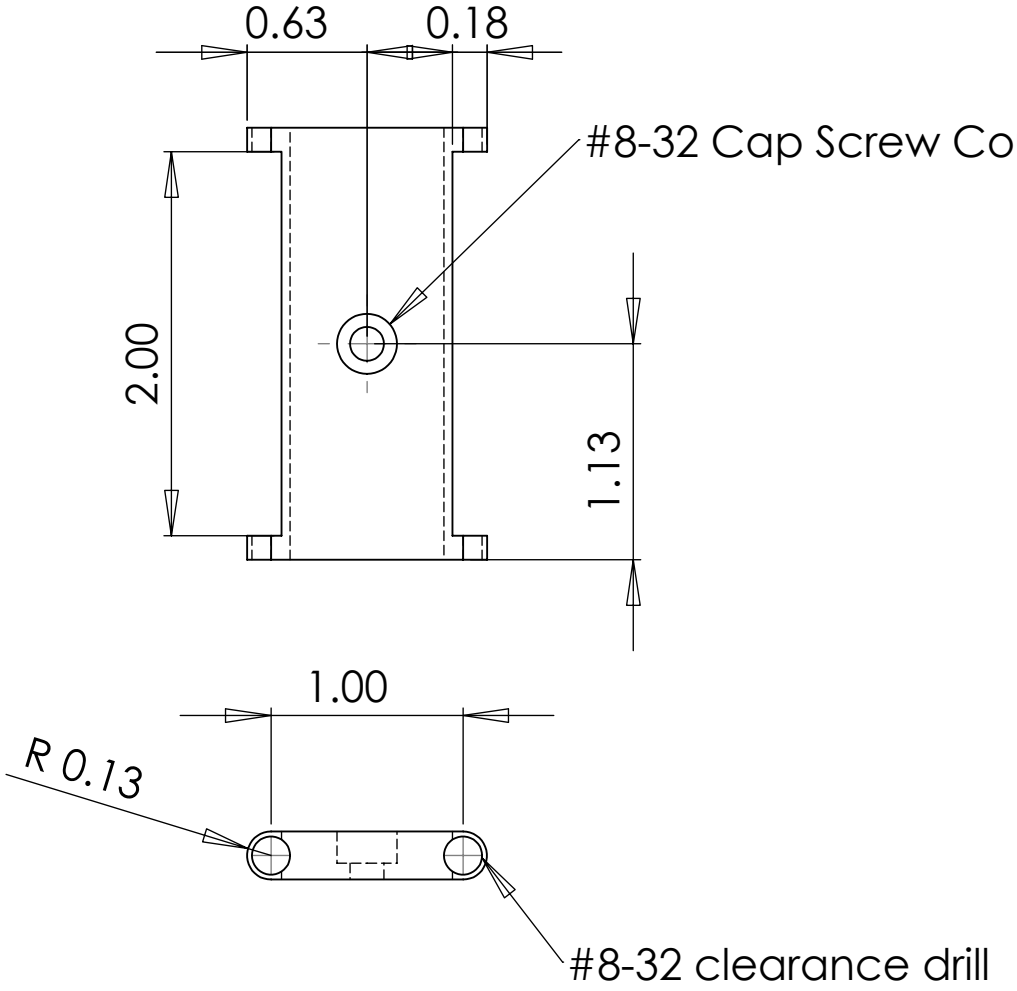

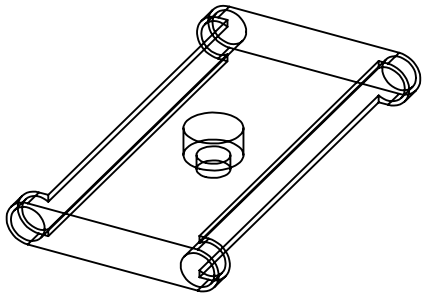

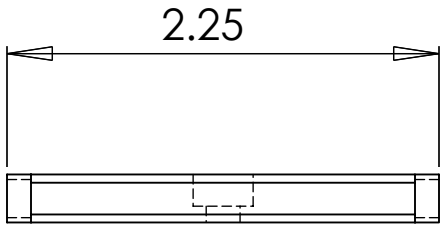

SCALE: 1:1

PART: TABLE CENTER
QUANTITY: 1
MATERIAL: ALUMINUM

Nature Methods: doi:10.1038/nmeth.1856

Supplementary Note 5

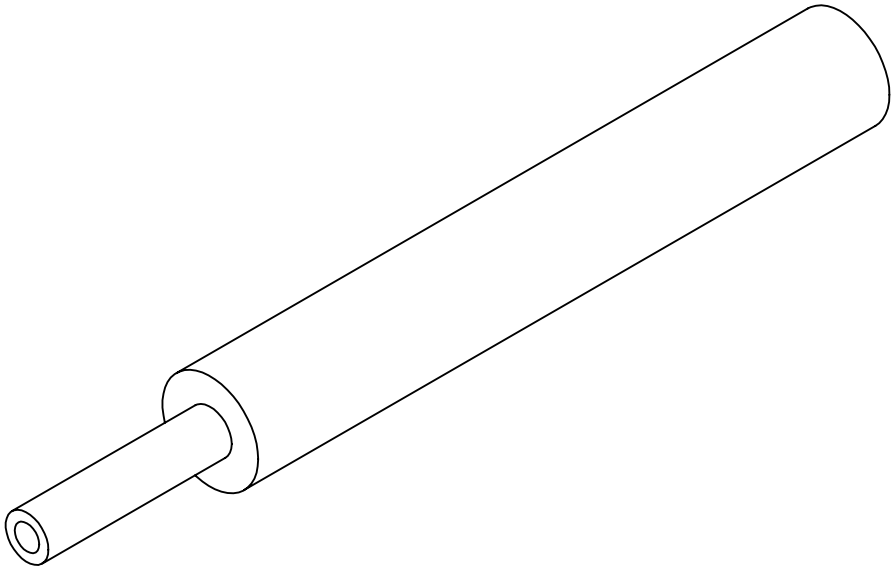

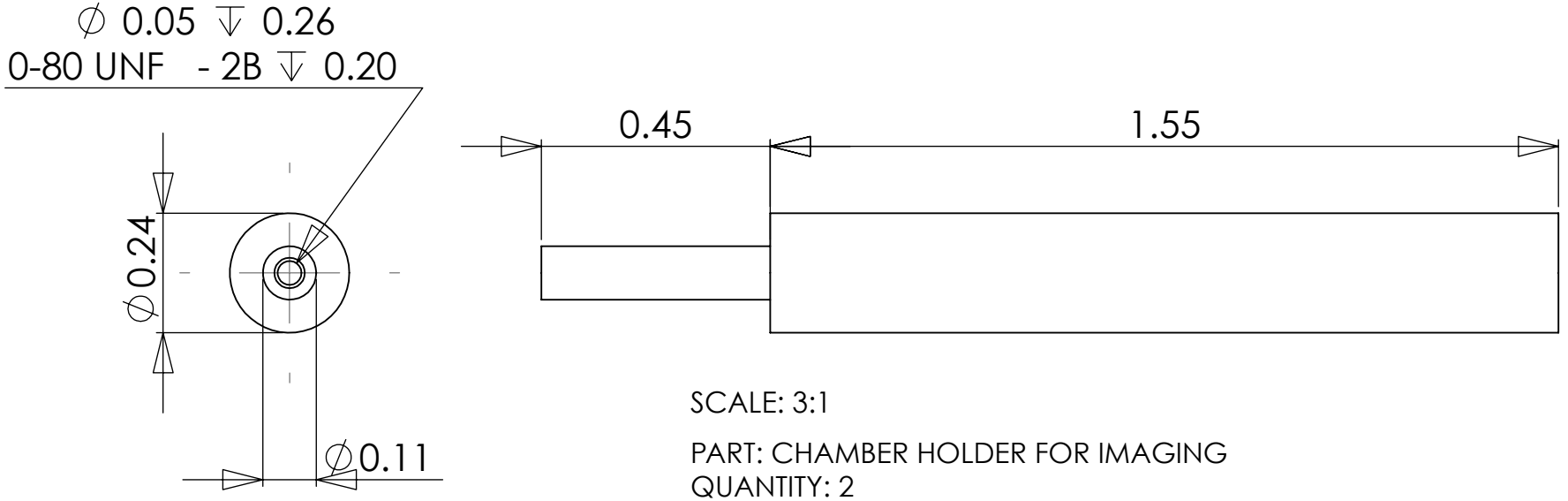

SCALE: 3:1

PART: CHAMBER HOLDER FOR IMAGING
QUANTITY: 2
MATERIAL: MODIFIED THOR LABS POST (STAINLESS STEEL)

Nature Methods: doi:10.1038/nmeth.1856

Supplementary Note 6

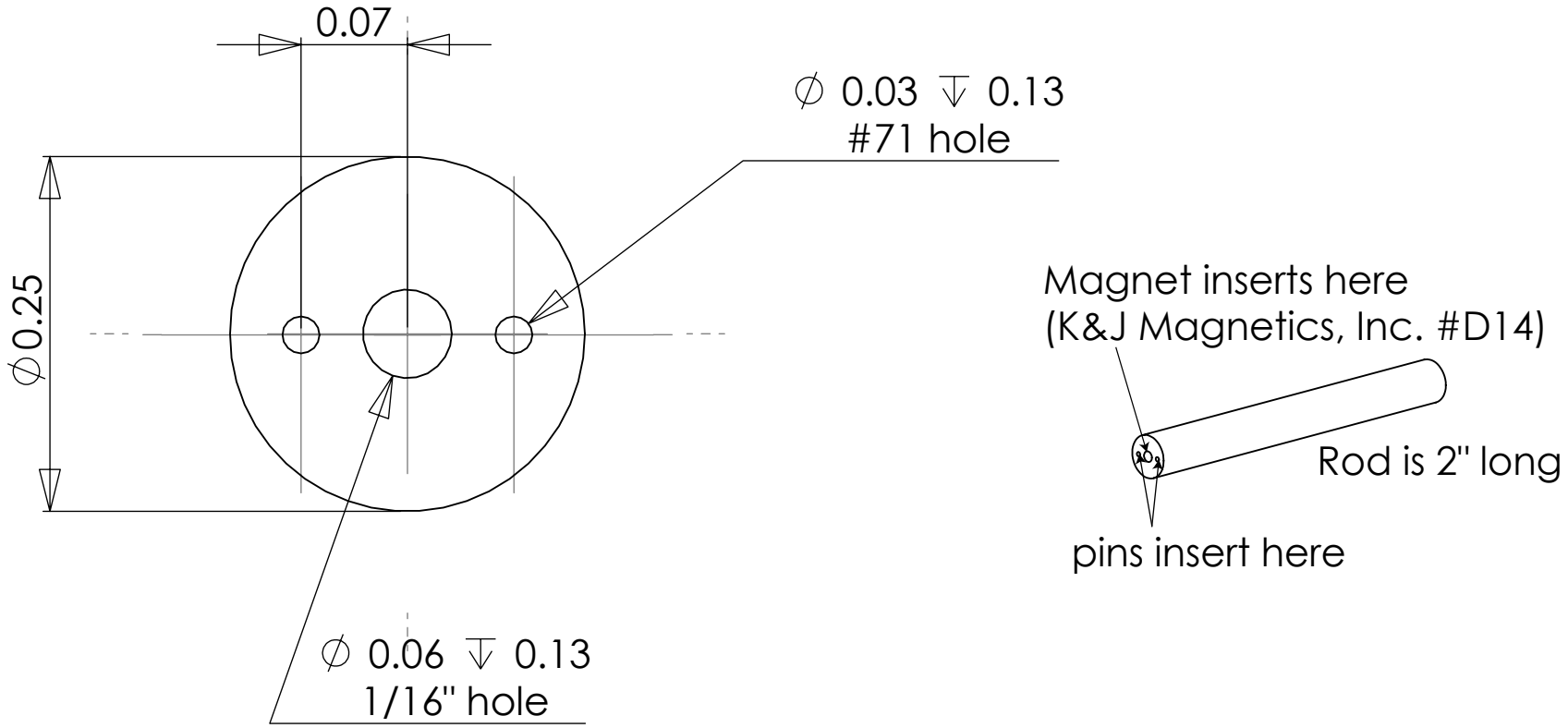

SCALE: 8:1

PART: BAR HOLDER FOR SURGERY
QUANTITY: 2
MATERIAL: MODIFIED THOR LABS POST (STAINLESS STEEL)

Nature Methods: doi:10.1038/nmeth.1856

Supplementary Protocol

1. A mouse is anesthetized on 5 % isoflurane mixed with 100 % oxygen in an induction chamber.
2. Once initial anesthesia has been achieved, the isoflurane is reduced to ~1.5-2 % for the duration of the procedure.
3. The mouse receives glycopyrrolate (0.05 mg per 100-g mouse), an anticholinergic, via intramuscular injection into the hindlimbs.
4. The mouse is transferred to a shaving/washing station away from the sterile surgery field where the relevant portions are shaved and receive three alternating washes of iodine and 70 % ethanol applied by cotton applicator.
5. The mouse receives 0.1 mL of 0.125 % bupivicaine, a local anesthetic, subcutaneously near the peak of the thoracic curvature. Between the ears or anywhere distal to the surgery site, 1 mL per 100-g mouse of 5 % glucose in saline, 0.25 mL per 100-g mouse of 0.5 mg/mL ketoprofen, and 0.2 mL per 100-g mouse of 0.1 mg/mL dexamethasone are administered by subcutaneous injection.
6. The mouse is transferred to custom spinal surgery table (Supplementary Fig. 3) with a feedback-controlled heating blanket overlaid with sterile drapes. All surgical tools should be sterilized by autoclaving or other suitable sterilization technique.
7. A small (~1 cm incision) is made with a #10 scalpel in the skin near the thoracic arch, and fascia connecting the skin to the underlying muscle is gentle pulled away using forceps.
8. Retractors are use to hold back the skin, creating an approimately ~1” x 1.5” exposed field.

9. After finding T11, T10 is firmly grasped through the muscle using forceps, and a scalpel is used in combination with a bone scraper to remove the muscle overlying T10-T12. Sterile cotton applicators are used to control bleeding as well as to gently remove tissue adhered to the bone.
10. Using curved scissors and forceps, tendons are severed from the transverse processes of vertebrae T10-T12.
11. Tissue lateral to the vertebral column is severed and retracted from the bone deep and wide enough to allow insertion of the side bars, but taking care not to injure the dorsal roots. Bleeding is controlled with sterile cotton applicators. Critical Step: To avoid necrosis, tissue must be trimmed smooth, especially along the transverse process of the vertebrae.
12. Side bars are delivered on custom 3-pronged post-holders (bar holder) and fuse the 3 vertebrae by clamping. The compression is held by tightening set screws on the right-angle post adapter.
13. Critical Step: It is essential that all soft tissue be effectively removed from T11. This can be achieved by drying the bone with cotton applicators and/or by applying a modest amount of cyanoacrylate glue and removing it after hardening, effectively providing a means of tissue debridement.
14. Vanna scissors are inserted just into the epidural space on either lateral aspect of the dorsal lamina of T11. If the bone is sufficiently dry, the initial cut should cause the bone to crack along its length.
15. The process is repeated for the contralateral side, and any rostral or caudal soft tissue is gently cut away while pulling the dorsal lamina away from the spinal cord with forceps.

Bleeding is controlled at the edges of the laminectomy using sterile cotton applicators. Blood is cleared from the spinal cord by flushing the exposed cord with artificial cerebrospinal fluid (ACSF). Critical Step: During the removal of the bone, part of the periosteum may detach and cover the spinal cord. This tissue should be delicately removed with a dural hook or small needle. Care should be taken to distinguish the periosteum from the dura mater.

16. Once the initial lamina is removed, carefully trim back the bone on the transverse processes to more fully expose the spinal cord. The surface of the bone may be sealed by carefully applying dental cement to both the bone surface and the side bars.

17. Once bleeding has been controlled and the spinal cord cleanly exposed, the top plate is positioned on top of the side bars and centered over the laminectomy.

18. Four #000-120 screws can then be partially inserted, starting with diagonally opposite slots. Once the final position is satisfactorily achieved, these screws may be tightened.

19. Kwik Sil elastomer is injected into the laminectomy site, taking care to avoid air bubbles.

20. Immediately after injection, a #0 cover slip is inserted to seal the laminectomy, gently applying pressure to squeeze the silicone into the rest of the chamber.

21. Approximately 10-20 minutes should be given to allow the silicone to set.

22. The silicone and chamber are sealed at the rostral and caudal edges by applying small amounts of dental acrylic and/or superglue to the chamber, silicone, and the exposed bone of T10 and T12.

23. The set screws on the right-angle adapters are loosened and the custom-delivery system is gently removed from the side bars.

24. Retractors are removed, and the skin is pulled up around the edges of the implant and secured with cyanoacrylate glue.
25. #0-80 set screws are inserted into the wings of the top plate.
26. Dental acrylic is applied on top of the skin at the edges of the implant and used to fill the slots in the top plate, providing a good seal on the chamber.
27. A second injection of 0.1 mL of 0.125 % bupivicaine is administered around the implant and the animal is transferred to a clean cage on a heat pad to recover.

Step-by-Step Imaging Procedure

1. The mouse is anesthetized on 5 % isoflurane mixed with 100 % oxygen in an induction chamber.
2. Once anesthesia has been achieved, the isoflurane is be reduced to ~1.5-2 % for the duration of imaging.
3. The mouse receives glycopyrrolate (0.05 mg per 100-g mouse), an anticholinergic, via intramuscular injection into the hindlimbs.
4. The mouse is transferred to the custom surgery table (Supplementary Figure 3) with a feedback-controlled heating pad.
5. Tapped posts (chamber holders) are inserted into the right-angle adapter and twisted onto the set screws on the wings of the chamber.
6. Set screws on the right-angle adapter are tightened to prevent the chamber from moving during imaging.

7. The posts are raised in the post-holders to elevate the thorax from the surgery table, thereby allowing for free expansion of the chest upon inspiration without introducing motion artifact. Set screws on the post-holders prevent up-down motion of the posts.
8. Vasculature is labeled by intravascular injection of a fluorescent dextran by retro-orbital injection. Briefly, a syringe is inserted under the eyeball with the bevel towards the nasal septum while dye is slowly ejected.
9. Multiphoton microscopy is performed for up to several hours.
10. The tapped posts (chamber holders) are unscrewed and the mouse is allowed to recover.

Trouble Shooting

Problem	Possible Reason	Solution
1. Chamber detaches from spinal cord post-surgically	• insufficient clamping pressure • insufficient gluing	• ensure appropriate pressure applied and that set screws in right-angle adapters are tight • apply glues more liberally at the rostral and caudal edges of the implant
2. Profuse bleeding in peripheral tissue during surgery.	• severing of major artery	• cauterize bleed with electro- or thermal cautery • apply pressure to bleed until stopped with cotton applicator
3. Air bubbles in silicone under window.	• air in mixer tip • air entering through edges of chamber	• ensure that air has been evacuated from the mixer tip prior to filling chamber • apply glues more liberally at the edge of the chamber to prevent silicone from pulling away from tissue • ensure that silicone has opportunity to set prior to disturbing the chamber
4. Blood in window post-surgery.	• bleeding in peripheral tissue entering under silicone • bleeding from vertebral body • bleeding from the spinal cord itself	• determine the source of bleeding by removing the silicone, and if necessary, replace it. • apply glues more liberally at the rostral and caudal edges of the implant to seal out any peripheral fluid from entering • ensure that the bone has stopped bleeding before applying silicone • carefully applying a thin layer of superglue to the bone can help reduce bone bleeds

Problem	Possible Reason	Solution
5. Rapid (few days) loss of image contrast	• fibrous tissue growth	• trim back more of transverse processes and seal with dental acrylic • reduce space for fibrous tissue to grow by minimizing the space between the glass and spinal cord by appropriate leveling of the implant
6. Motion artifact complicates imaging.	• chamber is loose • chamber is not securely held • mouse is insufficiently elevated • spinal cord moving within vertebral column	• ensure appropriate pressure is applied and that set screws in right-angle adapters are tight • apply glues more liberally at the rostral and caudal edges of the implant • ensure all set screws are tightly fastened • elevate mouse so that chest can expand freely upon inspiration

Supplementary Note 7: Equipment and Settings

Image(s): Figure 1a,d
Acquisition device: Canon DS12601 Digital Camera
Lens: Canon Macro Lens (EF 100 mm)
Photo Processing: image brightening, uniform linear contrast adjustment

Image(s): Figure 1c
Acquisition device: Canon DS12601 Digital Camera
Lens: Leica MZ12.5 Stereomicroscope
Photo Processing: image brightening, uniform linear contrast adjustment

Image(s): Figure 2a
Objective Lens: Zeiss 20x water immersion (NA = 1.0)
Original bit depth: 16 bit/color
Fluorphore(s): YFP, Texas Red
Excitation Wavelength: 1040 nm
Bandpass Emisssion Filters: 517/65 nm, 645/65
Dichroic: 600-nm long-pass
x-y resolution: 1.11 µm/pix
z increment: 1 µm/frame
z-projection type: standard deviation
Filtering: none

Image(s): Figure 2b
Objective Lens: Zeiss 20x water immersion (NA = 1.0)
Original bit depth: 16 bit
Excitation Wavelength: 1040 nm
Fluorphore(s): YFP
Bandpass Emisssion Filters: 517/65 nm
Dichroic: 600-nm long-pass

x-y resolution: 0.59 µm/pix
z increment: 0.5 µm/frame
z-projection type: standard deviation
Filtering: bandpass filtering (0-80 pixel)

Image(s): Figure 3a,b,c (insets)
Microscope: Olympus BX41
Objective Lens: Olympus UPlan Fl 20x/0.5
Original bit depth: 8 bit
Excitation Source: Halogen lamp
Bandpass Emisssion Filters: standard GFP filter cube
Field of View: 880 µm
Image processing: image cropping

Image(s): Figure 3c
Microscope: Olympus BX41
Objective Lens: Olympus UPlan Fl 4x/0.13
Original bit depth: 8 bit
Type: Bright field image
Field of View: 4.2 mm/panel
Image processing: image stitching (4 panels), image cropping

Image(s): Figure 4a-c
Objective Lens: Zeiss 20x water immersion (NA = 1.0)
Original bit depth: 16 bit/color
Fluorphore(s): YFP, GFP
Excitation Wavelength: 920 nm and 1040 nm
Bandpass Emisssion Filters: 517/65 nm, 550/50
Dichroic: 560-nm long-pass
x-y resolution: 0.59 µm/pix
z increment: 1 µm/frame

z-projection type: average
Filtering: linear unmixing

Image(s): Figure 5a
Objective Lens: Olympus 4x (NA = 0.28)
Original bit depth: 16 bit/color
Fluorphore(s): YFP, Texas Red
Excitation Wavelength: 1040 nm
Bandpass Emisssion Filters: 517/65 nm, 645/65
Dichroic: 600-nm long-pass
x-y resolution: 2.78 µm/pix
z increment: 5 µm/frame
z-projection type: standard deviation
Filtering: linear unmixing, image stitching (3 panels)

Image(s): Figure 5b
Objective Lens: Zeiss 20x water immersion (NA = 1.0)
Original bit depth: 16 bit
Fluorphore(s): YFP
Excitation Wavelength: 1040 nm
Bandpass Emisssion Filters: 517/65 nm, 645/65
Dichroic: 600-nm long-pass
x-y resolution: 0.59 µm/pix
z increment: 1 µm/frame
z-projection type: standard deviation
Filtering: bandpass filtering (0-80 pixel)

Image(s): Supplmentary Figure 1b,d,f,h
Acquisition device: Canon DS12601 Digital Camera
Lens: Leica MZ12.5 Stereomicroscope
Photo Processing: image brightening, uniform linear contrast adjustment

Image(s): Supplementary Figure 2
Acquisition device: Nikon P80 Digital Camera
Photo Processing: image brightening, uniform linear contrast adjustment

Image(s): Supplementary Figure 3
Objective Lens: Olympus 40x water immersion (NA = 0.8)
Original bit depth: 16 bit/color
Fluorphore(s): YFP, Texas Red
Excitation Wavelength: 1040 nm
Bandpass Emisssion Filters: 517/65 nm, 645/65
Dichroic: 600-nm long-pass
x-y resolution: 0.59 μm/pix
z increment: 1 μm/frame
z-projection type: standard deviation
Filtering: none

Image(s): Supplementary Figure 4
Objective Lens: Olympus 40x water immersion (NA = 0.8)
Original bit depth: 16 bit/color
Fluorphore(s): YFP, Texas Red
Excitation Wavelength: 1040 nm
Bandpass Emisssion Filters: 517/65 nm, 645/65
Dichroic: 600-nm long-pass
x-y resolution: 0.59 μm/pix
z increment: 0.5 μm/frame
z-projection type: standard deviation
Filtering: none